The Astrophysical Journal, 731:117 (17pp), 2011 April 20 doi:10.1088/0004-637X/731/2/117

CLUSTERING OF OBSCURED AND UNOBSCURED QUASARS IN THE BOÖTES FIELD: PLACING RAPIDLY GROWING BLACK HOLES IN THE COSMIC WEB

Ryan C. Hickox[1,2,12], Adam D. Myers[3], Mark Brodwin[2], David M. Alexander[1], William R. Forman[2], Christine Jones[2], Stephen S. Murray[2,4], Michael J. I. Brown[5], Richard J. Cool[6,13], Christopher S. Kochanek[7], Arjun Dey[8], Buell T. Jannuzi[8], Daniel Eisenstein[2,9], Roberto J. Assef[10,14], Peter R. Eisenhardt[10], Varoujan Gorjian[10], Daniel Stern[10], Emeric Le Floc'h[11], Nelson Caldwell[2], Andrew D. Goulding[1,2], and James R. Mullaney[1,11]

[1] Department of Physics, Durham University, South Road, Durham, DH1 3LE, UK; ryan.hickox@durham.ac.uk.
[2] Harvard-Smithsonian Center for Astrophysics, 60 Garden Street, Cambridge, MA 02138, USA
[3] Department of Astronomy, University of Illinois at Urbana-Champaign, Urbana, IL 61801, USA
[4] Department of Physics & Astronomy, The Johns Hopkins University, 3400 N. Charles Street, Baltimore, MD 21218, USA
[5] School of Physics, Monash University, Clayton 3800, Victoria, Australia
[6] Princeton University Observatory, Peyton Hall, Princeton, NJ 08544, USA
[7] Department of Astronomy, The Ohio State University, 140 West 18th Avenue, Columbus, OH 43210, USA
[8] National Optical Astronomy Observatory, Tucson, AZ 85726, USA
[9] Steward Observatory, 933 North Cherry Avenue, Tucson, AZ 85721, USA
[10] Jet Propulsion Laboratory, California Institute of Technology, Pasadena, CA 91109, USA
[11] Laboratoire AIM-Paris-Saclay, CEA/DSM/Irfu-CNRS-Université Paris Diderot, CE-Saclay, pt courrier 131, 91191 Gif-sur-Yvette, France
Received 2010 December 22; accepted 2011 February 18; published 2011 March 31

ABSTRACT

We present the first measurement of the spatial clustering of mid-infrared-selected obscured and unobscured quasars, using a sample in the redshift range $0.7 < z < 1.8$ selected from the 9 deg^2 Boötes multiwavelength survey. Recently, the *Spitzer Space Telescope* and X-ray observations have revealed large populations of obscured quasars that have been inferred from models of the X-ray background and supermassive black hole evolution. To date, little is known about obscured quasar clustering, which allows us to measure the masses of their host dark matter halos and explore their role in the cosmic evolution of black holes and galaxies. In this study, we use a sample of 806 mid-infrared-selected quasars and ≈250,000 galaxies to calculate the projected quasar–galaxy cross-correlation function $w_p(R)$. The observed clustering yields characteristic dark matter halo masses of $\log(M_{\rm halo}\ [h^{-1}\ M_\odot]) = 12.7^{+0.4}_{-0.6}$ and $13.3^{+0.3}_{-0.4}$ for unobscured quasars (QSO-1s) and obscured quasars (Obs-QSOs), respectively. The results for QSO-1s are in excellent agreement with previous measurements for optically selected quasars, while we conclude that the Obs-QSOs are *at least* as strongly clustered as the QSO-1s. We test for the effects of photometric redshift errors on the optically faint Obs-QSOs, and find that our method yields a robust lower limit on the clustering; photo-z errors may cause us to underestimate the clustering amplitude of the Obs-QSOs by at most ∼20%. We compare our results to previous studies, and speculate on physical implications of stronger clustering for obscured quasars.

Key words: galaxies: active – large-scale structure of universe – quasars: general – surveys

Online-only material: color figures

1. INTRODUCTION

Supermassive black holes with masses $\gtrsim 10^6\ M_\odot$ are ubiquitous in the nuclei of local galaxies of moderate to high mass (e.g., Kormendy & Richstone 1995). It is now well established that most of the total mass in black holes in the nearby universe was accreted in luminous episodes with high Eddington rates (e.g., Soltan 1982; Yu & Tremaine 2002), with the growth for massive ($M_{\rm BH} \gtrsim 10^8\ M_\odot$) black holes occurring predominantly at $z \gtrsim 1$ (e.g., Merloni & Heinz 2008; Shankar et al. 2009). These rapidly accreting black holes are most readily identified as bright optical quasars with characteristic broad (>1000 km s^{-1}) emission lines and luminous continuum emission that can dominate the light from the host galaxy, particularly at ultraviolet and optical wavelengths (e.g., Elvis et al. 1994; Richards et al. 2006; Schneider et al. 2007). Optical quasars thus provide powerful tools for tracing the rapid growth of black holes over cosmic time (e.g., Croom et al. 2004; Richards et al. 2005; Fan et al. 2006).

However, it is increasingly clear that a significant fraction of the quasar population does not show characteristic blue continua or broad lines because their nuclear emission regions are obscured. Key evidence for the existence of obscured (Type 2) quasars comes from synthesis models of the cosmic X-ray background (e.g., Comastri et al. 1995; Gilli et al. 2007a), as well as direct identification of these objects through various observational techniques. These include selection of luminous quasars with only narrow optical lines (Zakamska et al. 2003, 2004, 2005; Reyes et al. 2008) or relatively weak X-ray emission (Ptak et al. 2006; Vignali et al. 2006, 2010), detection of powerful radio galaxies lacking strong nuclear optical continua or broad lines (e.g., McCarthy 1993; Seymour et al. 2007), and detection of X-ray sources that are optically faint (e.g., Alexander et al. 2001; Stern et al. 2002; Treister et al. 2004; Mainieri et al. 2005), have hard X-ray spectra (e.g., Vignali et al. 2009), or have radio bright, optically weak counterparts (e.g., Martínez-Sansigre et al. 2006).

[12] STFC Postdoctoral Fellow.
[13] Hubble Fellow and Carnegie-Princeton Fellow.
[14] NASA Postdoctoral Program Fellow.

With the launch of the *Spitzer Space Telescope*, large numbers of obscured quasars can now be efficiently identified based on their characteristic (roughly power law) spectral energy distributions (SEDs) at mid-infrared (mid-IR) wavelengths ($\approx$3–24 μm). Because mid-IR emission is less strongly affected by dust extinction than optical and ultraviolet light, obscured quasars can appear similar to their unobscured counterparts in the mid-IR, but have optical emission characteristic of their host galaxies. A number of studies using mid-IR colors (Lacy et al. 2004; Stern et al. 2005; Rowan-Robinson et al. 2005; Hickox et al. 2007, hereafter H07), SED fitting (Alonso-Herrero et al. 2006; Donley et al. 2007), or selecting objects based on similarities to mid-IR quasar templates (e.g., Polletta et al. 2006) have been successful in identifying large numbers of dust-obscured quasars, indicating that a large fraction, and possibly a majority of rapid black hole growth is obscured by dust.

These large new samples enable detailed statistical studies that can explore the role of obscured quasars in galaxy and black hole evolution. At present, there are a number of possible physical scenarios for obscured quasars; in the simplest "unified models," obscuration is attributed to a broadly axisymmetric "torus" of dust that is part of the central engine, so obscuration is entirely an orientation effect (e.g., Antonucci 1993; Urry & Padovani 1995). Alternatively, obscuration may not be due to a central "torus" but to larger dust structures such as those predicted during major mergers of galaxies (e.g., Silk & Rees 1998; Springel et al. 2005; Hopkins et al. 2006a). Obscured quasars may represent an early evolutionary phase when the growing black hole cannot produce a high enough accretion luminosity to expel the surrounding material (e.g., Hopkins et al. 2008; King 2010), and such a phase of accretion may be concurrent with rapid star formation, as suggested for luminous dust-obscured galaxies (DOGs; Dey et al. 2008; Brodwin et al. 2008). Observations have revealed evidence for obscuration by a "torus" in some cases and by galactic-scale structures in others (e.g., Zakamska et al. 2005; Page et al. 2004; Martínez-Sansigre et al. 2009), and while there are examples of obscured quasars that show clear signs of radiative feedback on interstellar gas, it is unclear whether they are driving the galaxy-scale outflows invoked in evolutionary models (Greene et al. 2011). Thus, the physical nature of obscured quasars remains poorly understood, and analyses with large samples of mid-IR-selected quasars will be essential for a more complete understanding of rapidly growing, obscured black holes.

One particularly powerful observational tool is spatial clustering, which allows us to measure the masses of the dark matter (DM) halos in which quasars reside. Clustering studies of unobscured quasars have shown that the masses of quasar host halos are remarkably constant with cosmic time, with $M_{\rm halo} \sim 3\times10^{12}\,h^{-1}\,M_{\odot}$ over the large redshift range $0 < z \lesssim 5$ (e.g., Porciani et al. 2004; Croom et al. 2005; Coil et al. 2007; Myers et al. 2007; Shen et al. 2007; da Ângela et al. 2008; Padmanabhan et al. 2009; Ross et al. 2009). This lack of variation in halo mass implies that the bias factor (clustering relative to the underlying DM) is an increasing function of redshift, since the DM is more weakly clustered earlier in cosmic time. The characteristic $M_{\rm halo}$ provides a strong constraint on models of quasar fueling by the major mergers of gas-rich galaxies (e.g., Kauffmann & Haehnelt 2000; Springel et al. 2005; Hopkins et al. 2006b), secular instabilities (e.g., Mo et al. 1998; Bower et al. 2006; Genzel et al. 2008) or accretion of recycled cold gas from evolved stars (Ciotti & Ostriker 2007; Ciotti et al. 2010), and may be related to quasars' role in regulating star formation and the emergence of the red galaxy population in halos of roughly similar mass $\sim10^{12}$–$10^{13}\,h^{-1}\,M_{\odot}$ (e.g., Coil et al. 2008; Brown et al. 2008; Conroy & Wechsler 2009; Tinker & Wetzel 2010).

Despite the power of clustering measurements in understanding quasar populations, little is known about the clustering of obscured quasars. Some measurements of lower luminosity active galactic nuclei (AGNs) indicate no significant difference between obscured and unobscured sources (Constantin & Vogeley 2006; Li et al. 2006; Gandhi et al. 2006; Mandelbaum et al. 2009; Gilli et al. 2009; Hickox et al. 2009). However, these AGNs likely have different physical drivers compared to powerful quasars (e.g., Hopkins & Hernquist 2006). For obscured quasars at high luminosities ($L_{\rm bol} \sim 10^{46}$ erg s^{-1}) and high redshift ($z \gtrsim 1$), the clustering has remained largely unexplored.

In this paper, we present the first measurement of the clustering of mid-IR-selected obscured quasars and make direct comparisons to their unobscured counterparts. We use a large sample of quasars (both obscured and unobscured) in the redshift range $0.7 < z < 1.8$ selected on the basis of IRAC colors by H07, using data from the 9 deg^2 Boötes multiwavelength survey. We also employ a sample of $\approx$250,000 galaxies with good estimates of photometric redshift, and measure the two-point cross-correlation between quasars and galaxies. We utilize a novel method developed by Myers et al. (2009, hereafter M09) to derive the projected real-space projected cross-correlation function, making use of the full probability distributions for the photometric redshifts.

Throughout this paper, we assume a cosmology with $\Omega_{\rm m} = 0.3$ and $\Omega_{\Lambda} = 0.7$. For direct comparison with other works, we assume $H_0 = 70$ km s^{-1} Mpc^{-1} (except for comoving distances and DM halo masses, which are explicitly given in terms of $h = H_0/(100$ km s^{-1} Mpc$^{-1})$). In order to easily compare to estimated halo masses in other recent works on quasar clustering (e.g., Croom et al. 2005; Myers et al. 2006; da Ângela et al. 2008; Ross et al. 2009), we assume a normalization for the matter power spectrum of $\sigma_8 = 0.84$. Photometry is presented in Vega magnitudes. All quoted uncertainties are 1σ (68% confidence).

2. OBSERVATIONS

The 9 deg^2 survey region in Boötes covered by the NOAO Deep Wide-Field Survey (NDWFS; Jannuzi & Dey 1999) is unique among extragalactic multiwavelength surveys in its wide field and uniform coverage using space- and ground-based observatories. Extensive optical spectroscopy makes this field especially well suited for studying the statistical properties of a large number of AGNs (C. Kochanek et al. 2011, in preparation). Further details of the Boötes data set have been presented in previous papers (e.g., Hickox et al. 2007, 2009; Ashby et al. 2009).

Redshifts for this study come from the AGN and Galaxy Evolution Survey (AGES; C. Kochanek et al. 2011, in preparation) which used the Hectospec multifiber spectrograph on the MMT (Fabricant et al. 2005). We use AGES Data Release 2 (DR 2), which includes all the AGES spectra taken in 2004–2006. Details of the AGN redshifts are given in H07 and Hickox et al. (2009).

Optical photometry from NDWFS was used for the selection of AGES targets and to derive optical colors and fluxes for AGES sources. NDWFS images were obtained with the Mosaic-1 camera on the 4 m Mayall Telescope at Kitt Peak National Observatory, with 50% completeness limits of 26.7, 25.0,

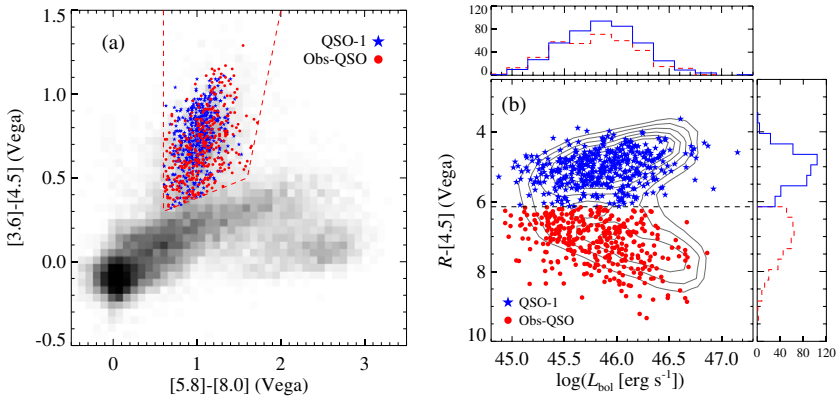

Figure 1. (a) IRAC color–color diagram showing the selection of the quasar samples using the criteria of Stern et al. (2005). The gray scale shows the density of sources detected at $>5\sigma$ significance in all four bands in IRAC Shallow Survey data. Blue stars and red circles show the QSO-1 and Obs-QSO samples, respectively. The Stern et al. (2005) color–color selection region is shown by the dashed line. (b) Illustration of the optical-IR color-selection criteria for dividing the IR-selected QSO sample into unobscured (QSO-1) and obscured (Obs-QSO) subsamples. Shown is the observed $R-[4.5]$ color vs. bolometric luminosity, calculated as described in Section 3.1. Contours show the distribution for all the H07 IR-selected quasars, while blue stars and red circles show the QSO-1 and Obs-QSO subsamples at $0.7 < z < 1.8$ used in this analysis as described in Section 3.1. The right and top panels show histograms of color and $L_{\rm bol}$, respectively, for the QSO-1s (blue solid line) and Obs-QSOs (red-dashed line). The contours and color histograms show that a simple cutoff in optical-IR color clearly separates the QSO samples into two populations, while the $L_{\rm bol}$ histograms demonstrate that the two samples are very closely matched in luminosity.

(A color version of this figure is available in the online journal.)

and 24.9 mag, in the B_W, R, and I bands, respectively. Photometry is derived using SExtractor (Bertin & Arnouts 1996).

Mid-infrared observations are taken from the *Spitzer* IRAC Shallow Survey (ISS; Eisenhardt et al. 2004), and *Spitzer* Deep Wide-Field Survey (SDWFS; Ashby et al. 2009). ISS covers the full AGES field in all four IRAC bands (3.6, 4.5, 5.8, and 8 μm), with 5σ flux limits of 6.4, 8.8, 51, and 50 μJy, respectively. The IRAC photometry for ISS is described in detail in Brodwin et al. (2006). The more recent SDWFS exposures extend these limits to 3.5, 5.3, 30, and 30 μJy, respectively. As discussed below, the quasar sample (as defined in H07) was selected using ISS data, while the galaxy sample for cross-correlation is selected from the full SDWFS data set. In computing bolometric luminosities for the quasars, we also make use of 24 μm flux measurements available from the Multiband Imaging Photometer for *Spitzer* (MIPS) GTO observations (IRS GTO team, J. Houck (PI), and M. Rieke) of the Boötes field. Significant fluxes ($>3\sigma$) were obtained for 97% of the quasars in our sample that lie in the region covered by MIPS.

3. QUASAR AND GALAXY SAMPLES

Our primary analysis is the two-point cross-correlation between mid-IR-selected quasars and galaxies. In this section, we give details of the quasar (both obscured and unobscured) and galaxy samples.

3.1. Quasar Sample

The quasars[15] are taken from the sample of luminous mid-IR-selected AGNs presented by H07. Quasars are identified on the basis of their colors in the mid-IR as observed by *Spitzer* IRAC, using the color–color criterion of Stern et al. (2005, Figure 1(a)), and are selected such that their best estimates of redshift are at $z > 0.7$. To the relatively shallow flux limits of the IRAC Shallow Survey, the AGN sample is highly complete and suffers little contamination from star-forming galaxies (as discussed in detail in Section 7 of H07; see also Assef et al. 2010, 2011).

H07 showed that at the ISS flux limits, the IR-selected quasars show a bimodal distribution in optical to mid-IR color. The selection boundary at $R-[4.5] = 6.1$ can be interpreted as dividing quasars into unobscured (optically bright and so "blue" in $R-[4.5]$) and obscured (optically faint and so "red" in $R-[4.5]$) subsets (Figure 1(b)). For the purposes of this study these objects will be referred to as "QSO-1s" and "Obs-QSOs," respectively; the reader is reminded that the selection is based not on optical spectroscopy but only on optical to mid-IR color. This selection yields samples of 839 QSO-1s and 640 Obs-QSOs at $z > 0.7$.

A detailed study of the optical colors, morphologies, and average X-ray spectra of these objects is given in H07. To briefly summarize, H07 found that the QSO-1s have blue optical colors, point-like optical morphologies, and soft X-ray spectra characteristic of unobscured quasars, while the Obs-QSOs had redder optical colors, extended optical morphologies, hard X-ray spectra, and high $L_{\rm X}$ characteristic of obscured quasars. The sample does not include all obscured quasars, as sources with very large extinction may fall below the IR flux limits of the survey or move out of the Stern et al. (2005) selection region (as shown in Figure 1 of H07; see also Gorjian et al. 2008; Assef et al. 2010). The typical absorbing column for the Obs-QSO sample is estimated to be $N_{\rm H} \sim 10^{22}$–10^{23} cm^{-2}. We expect the Obs-QSOs to suffer little contamination from bright star-forming galaxies. H07 used an X-ray stacking analysis and constraints from deeper surveys to estimate the possible contamination, and concluded that the contamination is at most $\approx$30%, and likely significantly smaller ($<$10%).

For our spatial correlation analysis, we limit the IR-selected quasar sample to the redshift range $0.7 < z < 1.8$ to maximize overlap with the normal galaxies in the field (Section 3.2). We also include only objects in regions of good optical photometry and away from bright stars. These criteria yield 563 QSO-1s and 361 Obs-QSOs. Finally, we restrict the QSO-1 sample to those spectroscopically identified as broad-line AGNs to ensure that

[15] We note that while H07 refers to the sample as "AGNs," their bolometric luminosities are estimated to be in the range 10^{45}–10^{47} erg s^{-1}, corresponding roughly to an X-ray luminosity range 5×10^{43} erg s$^{-1} \lesssim L_{\rm X} \lesssim 5 \times 10^{45}$ erg s^{-1} (Marconi et al. 2004; Hopkins et al. 2007). Such high-luminosity AGNs are typically referred to as "quasars" in the literature, so to avoid confusion with studies of lower luminosity active galaxies, here, we refer to our sample as "quasars."

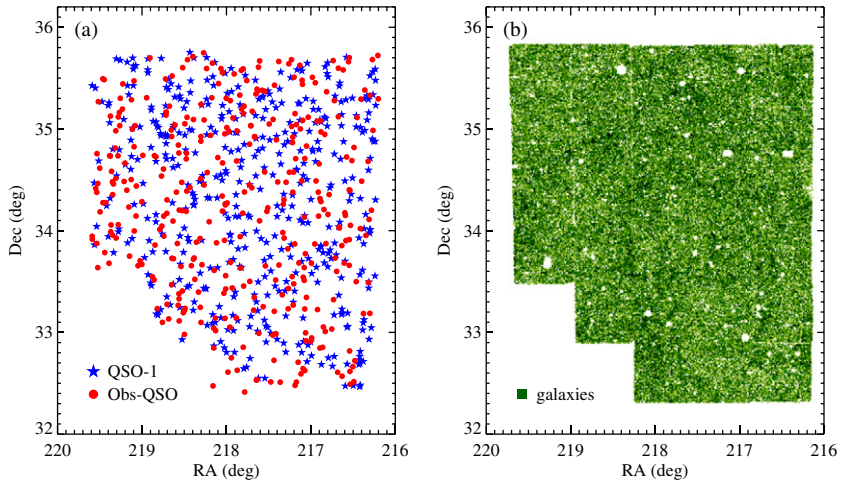

Figure 2. Left: sky positions of IR-selected quasars at $0.7 < z < 1.8$ in the Boötes field. Quasars are selected using the color–color criteria of Stern et al. (2005), and are divided into unobscured (QSO-1; blue stars) and obscured (Obs-QSO; red circles) as sources with optical-IR color blueward and redward, respectively, of the boundary $R - [4.5] = 6.1$. Right: surface density on the sky for the sample of 256,124 SDWFS galaxies at $0.5 < z < 2$. Objects in regions of unreliable photometry are excluded from both the quasar and galaxy data sets.

(A color version of this figure is available in the online journal.)

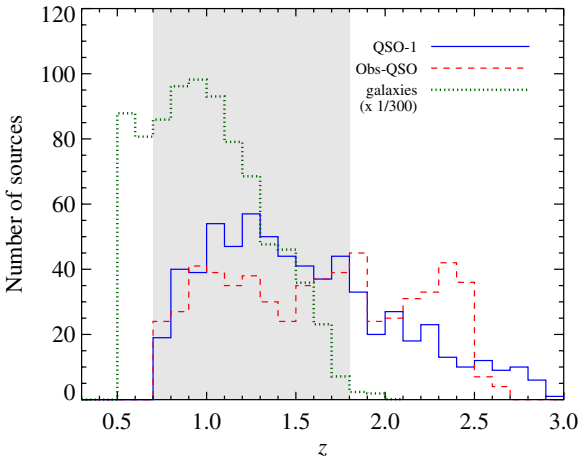

Figure 3. Redshift distributions for the photometric galaxy sample between at $0.5 < z < 2$ (green-dotted line), and the unobscured (blue solid line) and obscured (red-dashed line) quasar samples of H07. The histogram for galaxies is multiplied by 1/300 so that the distribution can be directly compared to that of the AGNs. The redshift range $0.7 < z < 1.8$ for which the correlation analysis is performed is shown by the shaded area. Redshift estimates for the galaxies and most of the Obs-QSOs are derived from the photometric redshift calculations using the method of Brodwin et al. (2006). The QSO-1s included in the correlation analysis have spectroscopic redshifts from MMT/Hectospec observations.

(A color version of this figure is available in the online journal.)

they unambiguously represent a sample of unobscured quasars and to enable clean tests of photo-z errors (see Section 6.3). Of the full sample of QSO-1s all redshifts, the vast majority (80%) have optical spectra from AGES and 96% of these are classified as broad-line AGNs at $0.7 < z < 4.3$, supporting their selection as unobscured quasars. We limit the QSO-1 sample to the 445 that have accurate optical spectroscopic redshifts in the range $0.7 < z < 1.8$ and clear broad emission line features. (In a sense this is conservative; we verify that including the 20% of objects with only photo-zs has no significant effect on the clustering results.) Based on these selection criteria, our QSO-1 sample is essentially equivalent to other Type 1 quasar samples selected purely on optical photometric colors and/or spectroscopy (e.g., Richards et al. 2001; Croom et al. 2004; Schneider et al. 2007; Richards et al. 2009b), since the vast majority of spectroscopic Type 1 quasars show AGN-like mid-IR colors (Stern et al. 2005; Richards et al. 2009a). The positions on the sky of the final samples of QSO-1s and Obs-QSOs are shown in Figure 2(a), and their distribution in redshift is given in Figure 3.

The Obs-QSOs are (by definition) optically faint, and so few (only 7%) are bright enough to obtain good redshifts from MMT optical spectroscopy. AGES targeted objects down to a flux limit of $I < 20$ for sources that are optically extended, which is the case for almost all the Obs-QSOs. Therefore, the vast majority of the Obs-QSO sample have only photometric estimates of redshift, derived using an artificial neural net technique (Brodwin et al. 2006). Uncertainties on photo-zs using this technique for optically bright quasars are typically $\sigma_z = 0.12(1 + z)$. However, the errors are more difficult to estimate for optically faint Obs-QSOs, for which there are few spectroscopic redshifts for comparison. Photo-z uncertainties were discussed at length by H07, with the conclusion that typical uncertainties are at most $\sigma_z = 0.25(1+z)$ and are likely smaller. Figure 4 shows the photo-zs and spec-zs for the handful of Obs-QSOs with spectroscopic redshifts, as well as those for the QSO-1s for comparison. The impact of photo-z errors in the present clustering analysis is addressed in detail in Section 6.3. As discussed in Section 6.3, random errors in the photo-zs can only tend to *decrease* the observed clustering amplitude, so we expect the present analysis to provide a robust lower limit on the clustering of the Obs-QSOs.

Since the primary aim of this analysis is to compare the clustering of quasars with and without obscuration by dust, it is imperative that the samples are otherwise matched in key properties such as redshift and luminosity. We show in Figure 3 that the redshift distributions of the two samples are similar, and we obtain bolometric luminosities ($L_{\rm bol}$) for the quasars by scaling from the rest-frame 8 μm luminosity. We compute the flux at rest-frame 8 μm by extrapolating between the fluxes at 8 and 24 μm in the observed frame, and use this flux to obtain the monochromatic luminosity νL_ν at 8 μm. We then multiply by a luminosity-dependent bolometric correction from Hopkins et al. (2007), which ranges from factors of $\approx$8 to 11, in order to obtain $L_{\rm bol}$. Visual inspection of the *Spitzer* data shows that essentially all of the quasars have broadly power-law SEDs at

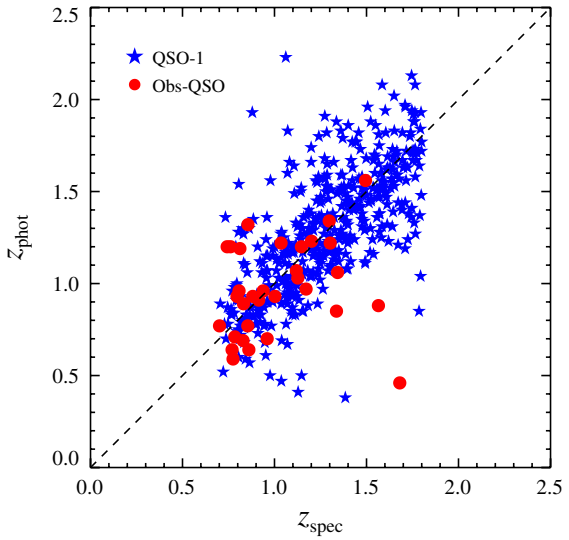

Figure 4. Photometric vs. spectroscopic redshift for the QSO-1 (blue stars) and Obs-QSO (red circles) IR-selected quasar samples. By selection, all the QSO-1s have spectroscopic redshifts, while the Obs-QSOs were generally too faint for optical spectroscopy. Only 19 Obs-QSOs have good optical redshifts; they are plotted here.

(A color version of this figure is available in the online journal.)

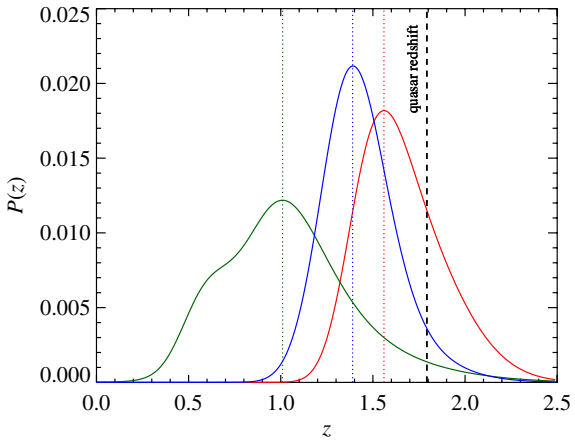

Figure 5. Sample PDFs for three galaxies in the SDWFS sample. Dotted lines show the "best" (peak) redshifts for each galaxy. The redshift of a sample quasar is shown by the dashed black line. Note that for the two lower redshift galaxies, the radial distance between the "peak" redshift of the galaxy and the quasar redshift are far too large for them to be physically associated. However, because of the uncertainty in the galaxy redshifts (shown by the PDFs), there is a non-negligible probability that the galaxies lie close to the radial distance of the quasar.

(A color version of this figure is available in the online journal.)

these wavelengths, indicating that the rest-frame 8 μm emission is indeed dominated by the AGN. We note that 49 quasars lie outside the region covered by the MIPS 24 μm observations, while 26 ($\approx$3%) of those inside the MIPS area are not detected at 24 μm. For these 75 objects, we use the estimates of L_{bol} derived from the rest-frame 2 μm luminosity as in Section 4.6 of H07[16].

The distributions in L_{bol} are almost identical for the QSO-1 and Obs-QSO samples, as shown in the top panel of Figure 1(b). The median and dispersion in $\log L_{bol}$ (erg s^{-1}) are (45.86, 0.37) and (45.83, 0.39) for QSO-1s and Obs-QSOs, respectively, indicating that the two samples are very well matched in bolometric luminosity. For completeness, we note that if we use the L_{bol} estimates derived from rest-frame 2 μm in H07 and restrict our analysis to QSO-1 and Obs-QSO samples that are matched in L_{bol}, this has a negligible effect on the clustering results.

3.2. Galaxy Sample

The sample of 256,124 galaxies is selected from the deeper SDWFS IRAC observations, with a flux limit [4.5] $<$ 18.6. The galaxies are selected to have best estimates of photometric redshift between 0.5 and 2, with an average photo-z of $\langle z \rangle = 1.09$. The sample includes an optical magnitude cutoff of $I < 24$ to restrict it to optical fluxes for which the photo-zs are well calibrated. To eliminate powerful AGNs, we have also excluded any object detected in 5 ks *Chandra* X-ray observations (Kenter et al. 2005) or with 5σ SDWFS detections in all four IRAC bands and colors in the Stern et al. (2005) AGN selection region. The exclusion of AGNs from the galaxy sample removes only 6979 objects and has negligible effect on the results.

[16] In general, the L_{bol} derived from the rest-frame 2 μm luminosity as used in H07 (which did not make use of the 24 μm data) broadly matches that obtained from the extrapolated 8 μm flux. However, the median L_{bol} obtained from 2 μm is smaller for the Obs-QSOs than for the QSO-1s by $\approx$0.15 dex, primarily because the Obs-QSOs have somewhat redder mid-IR SEDs consistent with the nuclear emission being reddened by dust (e.g., Haas et al. 2008).

The distribution on the sky of the 256,124 galaxies is shown in Figure 2(b), and their distribution in photometric redshift is shown in Figure 3. Photometric redshifts are obtained using an updated version of the Brodwin et al. (2006) algorithm, which is based on template fitting to the optical-IR SEDs. The SED fitting produces a redshift probability density function (PDF) for each object, where $P(z)$ represents the probability that the object lies at redshift z. (Note that the neural net used for the quasar photo-zs does not produce an equivalent estimate of the PDF. Thus, for the quasars we use the best value for the redshift, as discussed in Section 4.) $P(z)$ is normalized such that $\int P(z)dz = 1$. For most galaxies, the PDF is roughly Gaussian in shape, although often with a broader tail toward higher redshift. The typical redshift uncertainties are $\sigma_z \sim 0.1(1+z)$, and only a small fraction ($\approx$0.6%) of galaxies show multiple significant peaks in the PDF at different redshifts. Typical galaxy PDFs are shown in Figure 5.

In addition to the observed galaxy catalog, the correlation analysis requires a reference sample of objects with random sky positions, in order to compare the observed quasar–galaxy pair counts with the number expected for an uncorrelated distribution. We use a catalog of 8×10^6 random "galaxies" that is assigned to random positions in the regions of good photometry, reflecting the spatial selection function for the SDWFS galaxies.

4. CORRELATION ANALYSIS

In this section, we outline our methods for measuring the spatial cross-correlation between quasars and galaxies, the autocorrelation of the galaxies, and the absolute bias and characteristic DM halo masses.

4.1. Projected Correlation Function

To measure the spatial clustering of quasars, we can in principle derive the autocorrelation of the quasars themselves, or measure their *cross*-correlation with a sample of other objects (specifically, normal galaxies) at the same redshifts. Our quasar sample is too small to obtain sufficiently good measurements

of their autocorrelation function. However, cross-correlation with galaxies (of which there are $\simeq$300 times as many objects in the Boötes data set) allows far greater statistical power. Furthermore, cross-correlation requires knowledge only of the selection function for the galaxies, which is generally better constrained than that for AGNs. Cross-correlations of AGNs with galaxies have proved an effective technique in a number of previous studies (e.g., Croom et al. 2004; Adelberger & Steidel 2005; Serber et al. 2006; Li et al. 2006; Coil et al. 2007; Wake et al. 2008; Coil et al. 2009; Hickox et al. 2009; Padmanabhan et al. 2009; Mandelbaum et al. 2009; Mountrichas et al. 2009; Donoso et al. 2010; Krumpe et al. 2010).

For the present analysis, the uncertainties in the galaxy photo-zs restrict our ability to perform a full three-dimensional clustering analysis. However, making use of the quasar redshifts and the galaxy photo-z information, we can derive a projected spatial correlation function ($w_p(R)$, with R in comoving h^{-1} Mpc) that has both higher signal to noise, and a more straightforward physical interpretation than, for example, the purely angular correlation function $\omega(\theta)$.

The two-point correlation function $\xi(r)$ is defined as the probability above Poisson of finding a galaxy in a volume element dV at a physical separation r from another randomly chosen galaxy, such that

$$dP = n[1 + \xi(r)]dV, \tag{1}$$

where n is the mean space density of the galaxies in the sample. The projected correlation function $w_p(R)$ is defined as the integral of $\xi(r)$ along the line of sight,

$$w_p(R) = 2\int_0^{\pi_{\rm max}} \xi(R,\pi)d\pi, \tag{2}$$

where R and π are the projected comoving separations between galaxies in the directions perpendicular and parallel, respectively, to the mean line of sight from the observer to the two galaxies. By integrating along the line of sight, we eliminate redshift-space distortions owing to the peculiar motions of galaxies, which distort the line-of-sight distances measured from redshifts. $w_p(R)$ has been used to measure correlations in a number of surveys, for example, Sloan Digital Sky Survey (SDSS; Zehavi et al. 2005; Li et al. 2006; Myers et al. 2009; Krumpe et al. 2010), 2SLAQ (Wake et al. 2008), DEEP2 (Coil et al. 2007, 2008, 2009), Boötes (Hickox et al. 2009; Starikova et al. 2010), COSMOS (Gilli et al. 2009), and GOODS (Gilli et al. 2007b).

In the range of separations $0.3 \lesssim r \lesssim 50\,h^{-1}$ Mpc, $\xi(r)$ for galaxies and quasars is roughly observed to be a power law

$$\xi(r) = (r/r_0)^{-\gamma}. \tag{3}$$

For sufficiently large $\pi_{\rm max}$ such that we average over all line-of-sight peculiar velocities, $w_p(R)$ can be directly related to $\xi(r)$ (for a power-law parameterization) by

$$w_p(R) = R\left(\frac{r_0}{R}\right)^{\gamma} \frac{\Gamma(1/2)\Gamma[(\gamma-1)/2]}{\Gamma(\gamma/2)}. \tag{4}$$

We use Equation (4) to obtain power-law parameters for the observed correlation functions, to facilitate straightforward comparisons to other works. However, we note that a number of recent studies have shown evidence for separate terms in the correlation function owing to pairs of galaxies found within a single DM halo (the "one-halo" term), and from pairs in which each galaxy is in a different halo (the "two-halo" term; e.g., Zehavi et al. 2004; Zheng et al. 2007; Coil et al. 2008; Brown et al. 2008; Zheng et al. 2009). A halo occupation distribution (HOD) analysis accounting for both the one- and two-halo terms can provide valuable constraints on the distribution of objects within their DM halos; however, a full HOD calculation is beyond the scope of the present analysis.

To measure $w_p(R)$ for the quasar–galaxy cross-correlation, we employ the method developed by M09. This technique makes use of the full photo-z PDF for every galaxy, to weight quasar–galaxy pairs based on the probability of their being associated in redshift space. We describe the formalism briefly here, and refer the reader to M09 for further details.

4.2. Cross-correlation Method

For a set of spectroscopic quasars all at the same comoving distance χ_* from the observer, the angular cross-correlation between the (spectroscopic) quasars and (photometric) galaxies can be expressed in terms of the physical transverse comoving distance by (e.g., Shanks et al. 1983)

$$w_\theta(R) = \frac{N_R}{N_G}\frac{D_Q D_G(R)}{D_Q R_G(R)} - 1, \tag{5}$$

where R is the projected comoving distance for a given angular separation θ, such that $R = \chi_*\theta$. N_G and N_R are the total numbers of photometric galaxies and random galaxies, respectively, and $D_Q D_G$ and $D_Q R_G$ are the number of quasar–galaxy and quasar–random pairs, respectively, in each bin of R.

Defining the radial distribution function for the full galaxy sample as $f(\chi)$, where $\int f(\chi)d\chi = 1$, and assuming that $f(\chi)$ varies slowly at the redshifts of interest, then the angular correlation function $w_\theta(R)$ is related to the projected real-space correlation function $w_p(R)$ by

$$w_\theta(R) = f(\chi_*)w_p(R) \tag{6}$$

(for a derivation see Section 3.2 of Padmanabhan et al. 2009). As discussed in detail in M09, we can generalize the analysis such that the contribution to $w_p(R)$ is calculated individually for each quasar–galaxy pair, with $f_{i,j}$ defined as the average value of the radial PDF $f(\chi)$ for each photometric object i, in a window of size $\Delta\chi$ around the comoving distance to each spectroscopic object j. We use $\Delta\chi = 100\,h^{-1}$ Mpc to effectively eliminate redshift-space distortions, although the results are insensitive to the details of this choice.

In this case of weighting by pairs, we obtain, as in Equation (13) of M09:

$$w_p(R) = N_R N_Q \sum_{i,j} c_{i,j}\frac{D_Q D_G(R)}{D_Q R_G(R)} - \sum_{i,j} c_{i,j}, \tag{7}$$

where

$$c_{i,j} = f_{i,j} \Big/ \sum_{i,j} f_{i,j}^2. \tag{8}$$

We refer the reader to Section 2 of M09 for a detailed derivation and discussion of these equations.

M09 use Equation (7) to compute the cross-correlation between spectroscopic and photometric quasars from SDSS in the relatively narrow redshift bin $1.8 < z < 2.2$, corresponding to comoving distances $3400 \lesssim \chi \lesssim 3800\,h^{-1}$ Mpc; they obtain

a cross-correlation length $r_0 = 4.56 \pm 0.48\,h^{-1}$ Mpc, assuming $\gamma = 1.5$. (Note that M09 do not derive $\gamma = 1.5$, they assume it purely to describe their method. Higher values of gamma are typically obtained in the recent literature, and we obtain $\gamma \approx 1.8$ in the present work.) Our quasar sample spans a comparatively larger range in redshift ($0.7 < z < 1.8$, corresponding to $1750 \lesssim \chi \lesssim 3400\,h^{-1}$ Mpc).

We evaluate Equation (7) by calculating the $D_Q D_G / D_Q R_G$ term individually for each quasar. That is, for each quasar and each bin in separation R, we sum the redshift weights $c_{i,j}$ for galaxies in the given range of distance from the quasar, and divide by the number of random galaxies in the same distance range (note that this implies $N_Q = 1$ in Equation (7)). The advantage of this procedure is that it consists of a simple sum and accounts exactly for the comoving distance to each quasar. However, the calculation is limited by shot noise on small scales where we have small numbers of quasar–galaxy and quasar–random pairs. To check that this does not significantly affect the results, we also divide the quasar sample into bins of width $\Delta z = 0.1$ (over which the comoving distance variations are small enough that there is little mixing between bins in R), and calculate the $D_Q D_G / D_Q R_G$ term for all the N_Q quasars in the bin. We then average the $w_p(R)$ values for the different bins to obtain a mean $w_p(R)$ over the redshift range of interest. The resulting clustering amplitude differs by $\lesssim$10% (and in the majority of cases, $<$ a few percent) compared to evaluating Equation (7) treating each quasar separately. The choice of method does not affect any of our conclusions, but to account for these differences we conservatively include an additional 10% systematic uncertainty on the measurement of the clustering amplitude. Finally, we emphasize that we are averaging $w_p(R)$ over the whole redshift range of $0.7 < z < 1.8$. The validity of this procedure depends on the fact that the observed $w_p(R)$ varies slowly in the redshift range of interest, which we verify explicitly in Section 6.2.

4.3. Galaxy Autocorrelation

To estimate DM halo masses for the quasars, we calculate the relative bias between quasars and galaxies from which we derive the absolute bias of the quasars relative to DM. As discussed below, calculation of absolute bias (and thus halo mass) requires a measurement of the autocorrelation function of the SDWFS galaxies. The large sample size enables us to derive the clustering of the galaxies accurately from the angular autocorrelation function $\omega(\theta)$ alone. Although we expect the photometric redshifts for the SDWFS galaxies to be well constrained (as discussed in Section 3.2), by using the angular correlation function we minimize any uncertainties relating to individual galaxy photo-zs for this part of the analysis. The resulting clustering measured for the galaxies has much smaller uncertainties than that for the quasar–galaxy cross-correlation. To save computation time, for the galaxy autocorrelation analysis we use a significantly smaller random catalog with only 5×10^5 random "galaxies." This likely introduces some additional shot noise into the calculation of $\omega(\theta)$; however, since the resulting uncertainties are still far smaller than those for the quasar–galaxy cross-correlation, they are more than sufficient for the present analysis.

We calculate the angular autocorrelation function $\omega(\theta)$ using the Landy & Szalay (1993) estimator

$$\omega(\theta) = \frac{1}{RR}(DD - 2DR + RR), \quad (9)$$

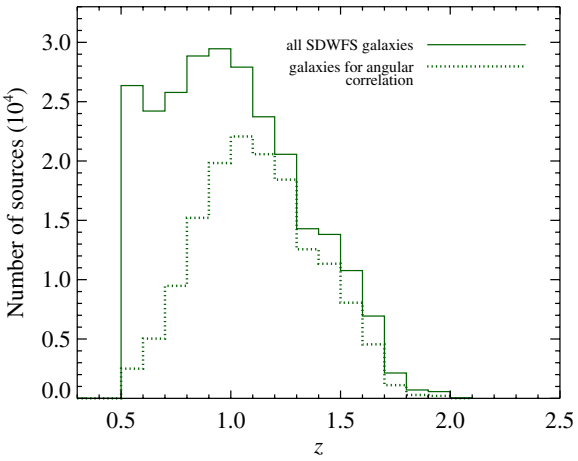

Figure 6. Redshift distribution for the full sample of 256,124 SDWFS galaxies (dotted line) and the sample of 151,256 galaxies selected to match the redshift overlap with the quasars, as described in Section 4.3 (solid line). The second galaxy sample is used to derive the angular autocorrelation of the galaxies (Section 4.3) as well as their angular cross-correlation with the quasars (Section 6.1).

(A color version of this figure is available in the online journal.)

where DD, DR, and RR are the number of data–data, data–random, and random–random galaxy pairs, respectively, at a separation θ, where each term is scaled according to the total numbers of quasars, galaxies, and randoms.

The galaxy autocorrelation varies with redshift, owing to the evolution of large-scale structure, and because the use of a flux-limited sample means that we select more luminous galaxies at higher z. This will affect the measurements of relative bias between quasars and galaxies, since the redshift distribution of the quasars peaks at higher z than that for the galaxies and so relatively higher z galaxies dominate the cross-correlation signal. To account for this in our measurement of galaxy autocorrelation, we randomly select galaxies based on the overlap of the PDFs with the quasars in comoving distance (in the formalism of Section 4.2 this is $f_{i,j}$ for each galaxy, averaged for all quasars). We select the galaxies so that their distribution in redshift is equivalent to the *weighted* distribution for all galaxies (weighted by $\langle f_{i,j} \rangle$). The redshift distribution of this galaxy sample is shown in Figure 6. We use this smaller galaxy sample to calculate the angular autocorrelation of SDWFS galaxies.

4.4. The Integral Constraint

In fields of finite size, estimators of the correlation function based on pair counts are subject to the integral constraint, which can be expressed as (Groth & Peebles 1977)

$$\int\int \omega(\theta_{12}) d\Omega_1 d\Omega_2 \simeq 0, \quad (10)$$

where θ_{12} is the angle between the solid angle elements $d\Omega_1$ and $d\Omega_2$ and the integrals are over the survey area. If the number density fluctuations in the volume are small, and the angular correlations are smaller than the variance within the volume, then to first order the correlation function is simply biased low by a constant equal to the fractional variance of the number counts. A straightforward way to remove this bias is to add to the observed $\omega(\theta)$ the term

$$\omega_\Omega = \frac{1}{\Omega^2} \int\int \omega(\theta_{12}) d\Omega_1 d\Omega_2, \quad (11)$$

where Ω is the area of the survey region. The value of $\bar{n}^2\omega_\Omega$, where $\bar{n}$ is an estimate of the mean number of galaxies per unit area, is the contribution of clustering to the variance of the galaxy number counts (Groth & Peebles 1977; Efstathiou et al. 1991). Evaluating Equation (11) for the Boötes survey area and the typical slope of the $\omega(\theta)$ for the objects considered here, we obtain $\omega_\Omega \approx 0.03\omega(1')$. We estimate $\omega(1')$ by interpolating the observed $\omega(\theta)$, then add ω_Ω to $\omega(\theta)$ before performing model fits. For the projected real-space correlation functions $w_p(R)$ (which is ultimately derived from individual estimates of $\omega(\theta)$, as in Equation (5)), we perform an approximate correction for the integral constraint. We determine the value of $w_p(R)$ at the physical scale (typically 0.5–1 h^{-1} Mpc) corresponding to $1'$ for each quasar, and add the average of these estimates (multiplied by 0.03) to the observed $w_p(R)$. These corrections increase the observed clustering amplitude by ≈10%, but have little effect on our overall conclusions.

4.5. Uncertainties and Model Fits

Ideally, uncertainties in $w_p(R)$ and $\omega(\theta)$ would be determined by calculating the correlation function for various random realizations of mock IR-selected quasar and galaxy samples, for example by populating DM N-body simulations. In the absence of such mock catalog, we instead determine uncertainties in $w_p(R)$ directly from the data through bootstrap resampling.

In a standard bootstrap analysis, the survey volume is divided into $N_{\rm sub}$ subvolumes, and these subvolumes are drawn randomly (with replacement) for inclusion in the calculation of the correlation function. Owing to the relatively small size of the field compared to large surveys such as SDSS or 2dF, we are only able to divide the field into a small number of subvolumes (we choose $N_{\rm sub} = 8$). The width of one subvolume corresponds to ≈50 h^{-1} Mpc at $z = 1.2$, so that correlations between the subvolumes should be relatively weak. (We verify explicitly that using a larger $N_{\rm sub} = 22$ has no significant effect on the results.) For each bootstrap sample draw a total of three $N_{\rm sub}$ subvolumes (with replacement), which has been shown to best approximate the intrinsic uncertainties in the clustering amplitude (Norberg et al. 2009). We then recalculate $w_p(R)$ including only the subvolumes in the bootstrap sample. For the calculations of $w_p(R)$, we use 10,000 bootstrap samples for which the uncertainties at each scale converge to better than 1%. (To save computing time, we limit the analysis to 2000 bootstrap samples for the angular correlation analyses, for which the uncertainties converge to within ≈1.5%.)

This bootstrap technique works well for the galaxy autocorrelation, for which we have a large number of objects and the uncertainty is dominated by the clustering of the sample rather than by counting statistics. However, for the quasar–galaxy cross-correlation, the bootstrap analysis results in very small errors that are significantly smaller than the observed scatter between points. This appears to be caused by the fact that, owing to the small quasar samples of only a few hundred objects, the uncertainties are dominated by shot noise that is not fully characterized by randomly selecting entire subvolumes. To account for the shot noise, we therefore take the sets of three $N_{\rm sub}$ bootstrap subvolumes and randomly draw from them (with replacement) a sample of objects (quasars or galaxies) equal in size to the parent sample; only pairs including these objects are used in resulting cross-correlation calculation. This procedure yields a good estimate of the shot noise (the resulting $\chi^2_\nu \sim 1$) while also accounting for covariance due to the large-scale structure.

When fitting power-law models to the observed correlation functions, we compute parameters by minimizing χ^2, taking into account covariance between different bins in R. From the bootstrap analysis, we can estimate the covariance matrix C_{ij} by

$$C_{ij} = \frac{1}{1-N}\left[\sum_{k=1}^{N}\left(w_p^k(R_i) - w_p(R_i)\right) \times \left(w_p^k(R_j) - w_p(R_j)\right)\right], \quad (12)$$

where $w_p^k(R_i)$ and $w_p^k(R_j)$ are the projected correlation function derived for the k-th bootstrap samples, N is the total number of bootstrap samples, and $w_p(R)$ is the correlation function for the full sample. This formalism is equally valid for bins of angular separation θ in calculations of $\omega(\theta)$. The 1σ uncertainty in each bin in R is the square root of the diagonal component of this matrix ($\sigma_i = (C_{ii})^{1/2}$).

Taking into account covariance, χ^2 is defined as

$$\chi^2 = \sum_{i=1}^{N_{\rm bins}}\sum_{j=1}^{N_{\rm bins}}\left(w_p(R_i) - w_p^{\rm model}(R_i)\right) \times C_{ij}^{-1}\left(w_p(R_j) - w_p^{\rm model}(R_j)\right), \quad (13)$$

where C_{ij}^{-1} is the inverse of the covariance matrix C_{ij}. We determine best-fit parameters by minimizing χ^2, and derive 1σ errors in each parameter by the range for which $\Delta\chi^2 = 1$. As a check, we also estimate parameter uncertainties by calculating best-fit parameters for each of the bootstrap samples and calculating the variance between them; this obtains almost identical estimates of the errors. Furthermore, we note that if we use only the diagonal terms in the covariance matrix in determining χ^2, the variation in the best-fit parameters is significantly smaller than the statistical uncertainties, indicating that the precise details of the covariance matrix are relatively unimportant.

We also note that while in principle the SDWFS field is large enough to enable measurements of clustering up to ∼50 h^{-1} Mpc at $z \sim 1$, we limit the analysis to scales $<12\,h^{-1}$ Mpc, because of edge effects that skew the correlation function on large scales but have minimal effect on smaller scales. An investigation of this effect is given in the Appendix.

4.6. Power-law Fits to Angular Correlation Functions

For the projected real-space quasar–galaxy cross-correlation analysis, we fit power-law models of $w_p(R)$ using Equation (4). We also fit power laws to the angular correlation functions (both galaxy autocorrelations and quasar–galaxy cross-correlations), using the simple expression

$$\omega(\theta) = A\theta^{-\delta}. \quad (14)$$

For meaningful comparison to other clustering measurements obtained using samples with different distributions in redshift, we wish to convert the observed parameters A and δ to the real-space r_0 and γ as defined in Equation (3). Inverting Limber's equation, the conversion between these parameters can be computed analytically (here we follow Section 4.2 of Myers et al. 2006; for the full derivation see Peebles 1980)

$$\gamma = \delta + 1 \quad (15)$$

$$A = H_\gamma \frac{\int_0^\infty (dN_1/dz)(dN_2/dz) E_z \chi^{1-\gamma} dz}{\left[\int_0^\infty (dN_1/dz) dz\right]\left[\int_0^\infty (dN_2/dz) dz\right]} r_0^\gamma, \quad (16)$$

where $H_\gamma = \Gamma(0.5)\Gamma(0.5[\gamma-1])/\Gamma(0.5\gamma)$, Γ is the gamma function, χ is the radial comoving distance, $dN_{1,2}/dz$ are the redshift distributions of the samples (for an autocorrelation $dN_1/dz = dN_2/dz$), and $E_z = H_z/c = dz/d\chi$. The Hubble parameter H_z can be found via

$$H_z^2 = H_0^2[\Omega_m(1+z)^3 + \Omega_\Lambda]. \quad (17)$$

Equation (16) assumes no evolution with redshift in the clustering of the sample (equivalent to the implicit assumption made in fitting $w_p(R)$ with Equation (4)). For each angular correlation analysis, we derive A and δ from the observed $\omega(\theta)$ and then obtain the corresponding γ and r_0 from Equations (15) and (16).

4.7. Absolute Bias and Dark Matter Halo Mass

The masses of the DM halos in which galaxies and quasars reside are reflected in their absolute clustering bias relative to the DM distribution. To determine absolute bias (following e.g., Myers et al. 2007; Coil et al. 2008; Hickox et al. 2009) we first calculate the two-point autocorrelation of DM as a function of redshift. We use the HALOFIT code of Smith et al. (2003) to determine the nonlinear-dimensionless power spectrum $\Delta^2_{\rm NL}(k,z)$ of the DM assuming our standard cosmology, and the slope of the initial fluctuation power spectrum, $\Gamma = \Omega_m h = 0.21$. The Fourier transform of the $\Delta^2_{\rm NL}(k,z)$ gives us the real-space correlation function $\xi(r)$, which we then integrate to $\pi = 100\,h^{-1}$ Mpc following Equation (2) to obtain the DM projected correlation function $w_p^{\rm DM}(R,z)$. The uncertainty in the DM power spectrum obtained from HALOFIT is $\sim$5%; this corresponds to a systematic uncertainty $\sim$0.05 dex in $M_{\rm halo}$, but does not impact the relative halo masses of the different subsamples.

To derive quasar absolute bias from the projected real-space correlation function, we average the $w_p^{\rm DM}(R)$ over the redshift distribution of the sample, weighted by the overlap with the galaxy PDFs. The overlap of each quasar with the galaxy PDFs is given by

$$W_i = \sum_j f_{i,j} \quad (18)$$

and the corresponding $w_p(R)$ for the DM is given by

$$w_p^{\rm DM}(R) = \sum_i W_i w_p^{\rm DM}(R, z_i) \Big/ \sum_i W_i, \quad (19)$$

where z_i is the quasar redshift.

The redshift distributions for the QSO-1s and Obs-QSOs are essentially identical (the resulting $w_p^{\rm DM}(R)$ values for the two samples differ by <2% on all scales), so for simplicity we use the same $w_p^{\rm DM}(R)$ (defined for the QSO-1s) for both sets of quasars. We obtain the bias by calculating the average ratio between the best-fit power-law model and $w_p^{\rm DM}(R)$ over the range of scales of 1–10 h^{-1} Mpc, for which $w_p^{\rm DM}(R)$ corresponds closely to a power law and is dominated by the two-halo term. The observed clustering amplitude relative to the DM corresponds to $b_Q b_G$, where b_Q and b_G are the absolute linear biases of the quasars and SDWFS galaxies, respectively.

To measure b_G from the galaxy autocorrelation function (or $b_Q b_G$ from the quasar–galaxy angular cross-correlation, described in Section 6.1), we require an estimate of the corresponding $\omega(\theta)$ of the DM. To obtain $\omega(\theta)$, we use Limber's equation to project the power spectrum $\Delta^2_{\rm NL}(k,z)$ into the angular correlation (Limber 1953; Peebles 1980; Peacock 1991; Baugh & Efstathiou 1993). Specifically, we perform a Monte Carlo integration of Equation (A6) of Myers et al. (2007) to obtain $\omega(\theta)$ for the DM. The key parameter in this equation is $(dN_G/dz)^2$ where dN_G/dz is the redshift distribution of the galaxies. We calculate dN_G/dz from the sum of the PDFs of the galaxies for which we perform the autocorrelation. In deriving the DM $\omega(\theta)$ for the quasar–galaxy cross-correlation, we replace $(dN/dz)^2$ with $(dN_Q/dz)(dN_G/dz)$, where dN_Q/dz is the distribution of quasar redshifts. For each angular correlation analysis, we compute the average ratio between the best-fit power-law model and the DM $\omega(\theta)$ on scales 1′–10′, where $\omega(\theta)$ is dominated by the two-halo term. This ratio yields b_G^2 for galaxy autocorrelations or $b_Q b_G$ for quasar–galaxy cross-correlations.

Finally, we use b_Q and b_G to estimate the characteristic mass of the DM halos hosting each subset of galaxies or quasars. Sheth et al. (2001) derive a relation between dark matter halo mass and large-scale bias that agrees well with the results of cosmological simulations. We use Equation (8) of Sheth et al. (2001) to convert $b_{\rm abs}$ to $M_{\rm halo}$ for the mean redshift of each subset of objects. If we use a different relation between $b_{\rm abs}$ and $M_{\rm halo}$ (Tinker et al. 2005), we obtain estimates for $M_{\rm halo}$ that are similar, although slightly larger by 0.2–0.3 dex; these differences do not significantly affect our conclusions.

We note that to estimate $M_{\rm halo}$, we have performed fits to the observed $w_p(R)$ on scales of 0.3–12 h^{-1} Mpc. In principle, the DM and galaxy correlation functions can have somewhat different shapes such that the bias depends on the range of scales considered. If we limit the fits on scales 1–12 h^{-1} Mpc, the results change by $\lesssim$5%, but with slightly larger uncertainties. We also note that our estimates of $M_{\rm halo}$ are relatively insensitive to our choice of σ_8. If we change σ_8 from 0.84 to 0.8 (as favored by the more recent *Wilkinson Microwave Anisotropy Probe* cosmology, e.g., Spergel et al. 2007) our $M_{\rm halo}$ estimates for quasars and galaxies increase by $\approx$0.1 dex.

5. RESULTS

In this section, we discuss the results of the correlation analysis and the characteristic DM halo masses for galaxies and quasars. We first calculate the cross-correlation of the full QSO-1 and Obs-QSO samples with SDWFS galaxies. The resulting $w_p(R)$ values and best-fit models are shown in Figure 7, and fit parameters are given in Table 1. For both sets of the quasars, the observed real-space projected cross-correlation is highly significant on all scales from 0.1–12 h^{-1} Mpc, and the power-law fits return $\gamma \approx 1.8$, similar to many previous correlation function measurements for quasars (e.g., Coil et al. 2007; Ross et al. 2009) and galaxies (e.g., Zehavi et al. 2005; Coil et al. 2008). The best-fit parameters are $r_0 = 5.4 \pm 0.7\,h^{-1}$ Mpc and $\gamma = 1.8 \pm 0.1$ for the QSO-1s, and $r_0 = 6.4 \pm 0.8\,h^{-1}$ Mpc and $\gamma = 1.7 \pm 0.1$ for the Obs-QSOs. The results indicate that the cross-correlation of the Obs-QSOs with galaxies is somewhat stronger than that for the QSO-1s. The corresponding values of $b_Q b_G$ are given in Table 1.

As a check, we also perform power-law fits to $w_p(R)$ but leaving the slope fixed to $\gamma = 1.8$, which corresponds to the slope of the $w_p(R)$ for the DM. This also yields a significant difference in the clustering amplitude, although somewhat

Table 1
Correlation Results

Subset	N_{src}[a]	$\langle z \rangle$[b]	Power-law Fit			Bias[c]		Halo Mass[c]
			r_0 (h^{-1} Mpc)	γ	χ^2_ν	$b_{abs}b_G$	b_{abs}	($\log h^{-1} M_\odot$)
Projected Real-space Cross-correlation ($w_p(R)$)[d]								
QSO-1	445	1.27	5.4 ± 0.7	1.8 ± 0.1	1.1	3.63 ± 0.92	2.17 ± 0.55	$12.7^{+0.4}_{-0.6}$
Obs-QSO	361	1.24	$6.4^{+0.7}_{-0.8}$	1.7 ± 0.1	1.2	5.11 ± 1.16	3.06 ± 0.70	$13.3^{+0.3}_{-0.4}$
$w_p(R)$ with Fixed γ[d]								
QSO-1	445	1.27	5.3 ± 0.6	1.8	1.1	3.44 ± 0.75	2.06 ± 0.45	$12.6^{+0.4}_{-0.5}$
QSO-1 (photo-z)	445	1.27	4.9 ± 0.6	1.8	1.2	3.05 ± 0.67	1.82 ± 0.40	$12.5^{+0.4}_{-0.6}$
Obs-QSO	361	1.24	6.0 ± 0.7	1.8	1.2	4.38 ± 0.84	2.62 ± 0.51	$13.0^{+0.3}_{-0.4}$
Angular Correlation ($\omega(\theta)$)[e]								
Galaxies	151256	1.10	4.7 ± 0.2	1.67 ± 0.05	1.1	2.79 ± 0.16	1.67 ± 0.05	12.30 ± 0.06
QSO-1	445	1.27	5.6 ± 0.8	1.8	1.1	4.19 ± 1.07	2.50 ± 0.65	$13.0^{+0.4}_{-0.6}$
Obs-QSO	361	1.24	6.0 ± 1.0	1.8	1.2	4.80 ± 1.29	2.87 ± 0.77	$13.2^{+0.3}_{-0.5}$

Notes.
[a] Number of objects included in the correlation analysis. For quasar–galaxy cross-correlation, we use the full sample of 256,124 galaxies (for $w_p(R)$ calculations) or 151,256 galaxies (for $\omega(\theta)$ calculations).
[b] Median redshift for the objects included in the correlation analysis.
[c] Uncertainties in the DM power spectrum introduce an additional systematic error of ~5% in b_{abs} (and corresponding ~0.05 dex in M_{halo}). Further systematic errors in M_{halo} of ~0.2 dex are caused by uncertainty in σ_8 and in the conversion from b_{abs} to M_{halo}, as discussed in Section 4.7. However, these do not significantly effect the *relative* halo masses, so these uncertainties is not included here. Note that for fits with fixed γ, uncertainties on r_0, bias, and M_{halo} do not account for covariance with γ and thus somewhat underestimate the error on the clustering amplitude.
[d] Real-space projected cross-correlation between quasars and galaxies, calculated as described in Section 4. For all $w_p(R)$ calculations, error estimates for r_0, bias, and M_{halo} include a 10% systematic uncertainty on the amplitude as described in Section 4.2.
[e] Angular galaxy autocorrelation and quasar–galaxy cross-correlation, calculated as described in Section 4.

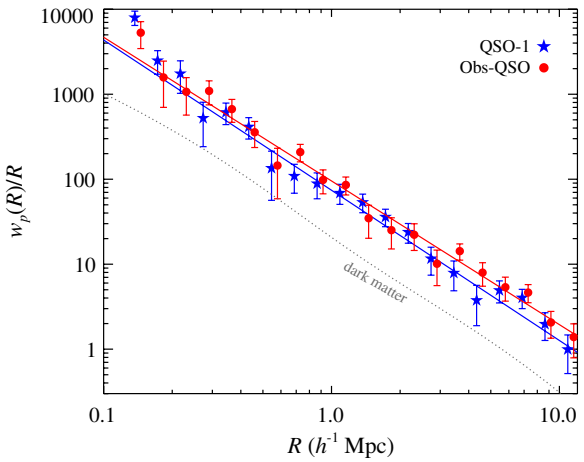

Figure 7. Projected quasar–galaxy cross-correlation function (derived using Equation (7)) for the QSO-1 (blue stars) and Obs-QSO (red circles) samples. Uncertainties are estimated from bootstrap resampling. Data points for the two quasar types are slightly offset for clarity. Power-law fits to $w_p(R)$ are shown as solid lines in blue (QSO-1s) and red (Obs-QSOs), and the projected correlation function for DM is shown by the dotted gray line. Fits are performed over the range in separation of $0.3 < R < 12\,h^{-1}$ Mpc.
(A color version of this figure is available in the online journal.)

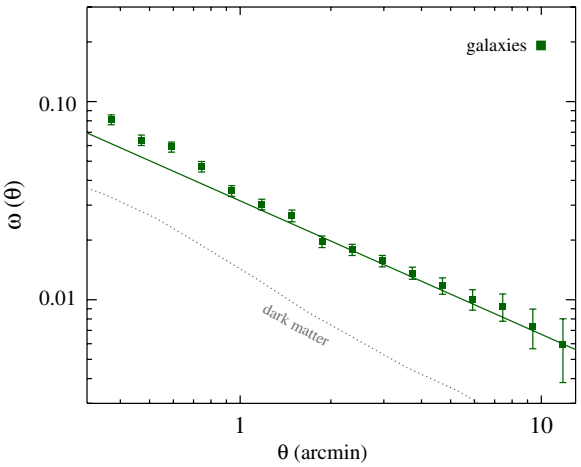

Figure 8. Angular autocorrelation function of SDWFS galaxies, selected to match the overlap of the quasars and galaxies in redshift space. Uncertainties are estimated from bootstrap resampling. The angular correlation function for DM, evaluated for the redshift distributions of the galaxies, is shown by the dotted gray line. The power-law fit was performed on scales 1′–12′ and is shown as the solid line. The excess in $\omega(\theta)$ at $\theta \lesssim 1'$ is due to the one-halo term arising from pairs of galaxies within the same DM halos (e.g., Quadri et al. 2008; Kim et al. 2011).
(A color version of this figure is available in the online journal.)

smaller, with $r_0 = 5.3 \pm 0.6$ and $r_0 = 6.0 \pm 0.6\,h^{-1}$ Mpc for the QSO-1s and Obs-QSOs, respectively. (Note that the formal uncertainties in r_0 here are smaller than for the above results because they do not account for covariance with γ.)

To obtain the absolute bias of SDWFS galaxies (b_G) in order to extract the quasar bias b_Q from the cross-correlation results, we next derive the autocorrelation of SDWFS galaxies for the sample described in Section 4.3. The observed $\omega(\theta)$ is shown in Figure 8, along with the correlation function for DM, calculated as discussed in Section 4.7. Fit parameters are given in Table 1. The power-law model fits well on the chosen scales of 1′–12′, although there is a clear excess corresponding to the one-halo term at $\theta < 1'$, as is common in galaxy autocorrelation measurements (e.g., Quadri et al. 2008; Kim et al. 2011). The best-fit power-law parameters are $r_0 = 4.7 \pm 0.2$ and

$\gamma = 1.67 \pm 0.05$, and the ratio of the best-fit power law to the DM $\omega(\theta)$ yields $b_G^2 = 2.79 \pm 0.16$ or $b_G = 1.67 \pm 0.05$.

This accurate value for b_G allows us to estimate b_Q for both types of quasars, based on the cross-correlation measurements. We obtain $b_Q = 2.17 \pm 0.55$ and 3.06 ± 0.70, for QSO-1s and Obs-QSOs, respectively. Converting these to DM halo masses using the prescription of Sheth et al. (2001) as described in Section 4.7, we arrive at $\log(M_{\rm halo}[h\,M_\odot^{-1}]) = 12.7^{+0.4}_{-0.6}$ and $13.3^{+0.3}_{-0.4}$ for QSO-1s and Obs-QSOs, respectively. The difference is marginally significant ($\approx 1\sigma$, although as we discuss below, the Obs-QSO clustering may represent only a robust lower limit).

For direct comparison with other studies that directly measure the quasar autocorrelation, it is useful to present the quasar clustering in terms of effective power-law parameters for their autocorrelation. Assuming linear bias, the quasar autocorrelation can be inferred from the cross-correlation by $\xi_{QQ} = \xi_{QG}^2/\xi_{GG}$ (e.g., Coil et al. 2009). We can therefore use the power-law fits to the quasar–galaxy cross-correlation and galaxy autocorrelation to derive an effective r_0 and γ for the quasar autocorrelation. This yields $r_0 = 6.1^{+1.4}_{-1.6}\,h^{-1}$ Mpc and $\gamma = 1.9^{+0.3}_{-0.2}$ for the QSO-1s and $r_0 = 8.8^{+2.0}_{-2.3}\,h^{-1}$ Mpc and $\gamma = 1.7 \pm 0.2$ for the Obs-QSOs. The autocorrelation amplitude and $M_{\rm halo}$ for QSO-1s are in excellent agreement with previous estimates for unobscured quasars, while the best-fit amplitude for Obs-QSOs is higher than most previous measurements of quasar clustering. We compare these results to previous work and discuss possible interpretations in Section 7.

6. VERIFICATION

In this section, we perform several tests to verify the validity of the clustering analysis outlined in Section 4. We first calculate the quasar–galaxy cross-correlation using a simple angular correlation function, minimizing dependence on the photometric redshifts. We then check for variation in the observed clustering over the redshift range of interest and confirm that any variation is relatively weak. Finally, we estimate the effects of uncertainties on the photometric redshifts on the observed real-space clustering amplitude for the Obs-QSOs. These checks confirm that our projected correlation analysis provides a robust estimate of the quasar–galaxy cross-correlation.

6.1. Angular Cross-correlation

We first calculate the cross-correlation of quasars and SDWFS galaxies using a simple angular clustering analysis, and check whether the corresponding absolute bias is consistent with that derived from the more sophisticated $w_p(R)$ calculation. To calculate the $\omega(\theta)$, we use an estimator corresponding to Equation (9) but for cross-correlations:

$$\omega(\theta) = \frac{1}{RR}(D_Q D_G - D_Q R - D_G R + RR), \qquad (20)$$

where each term is scaled according to the total numbers of galaxies and randoms. To maximize the signal-to-noise ratio by cross-correlating objects associated in redshift space, the galaxies include only the redshift-matched SDWFS sample of 151,256 objects described in 4.3. Uncertainties are estimated using bootstrap resampling as described in Section 4.5. We fit the observed cross-correlation with a power law as described in Section 4.6. Owing to the limited statistics which provide only very weak constraints on the power-law slope, we fix $\delta = 0.8$ (corresponding to real-space $\gamma = 1.8$).

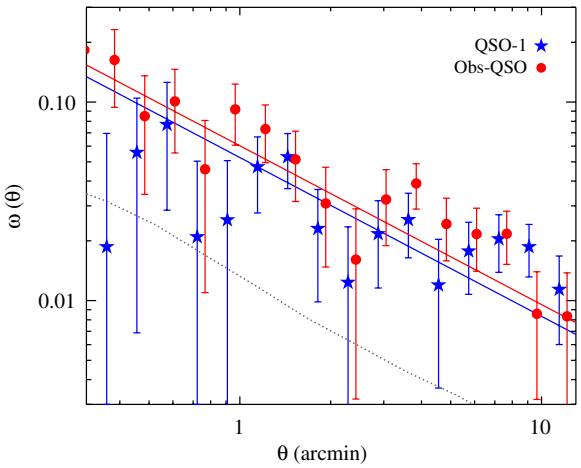

Figure 9. Angular quasar–galaxy cross-correlation function for the QSO-1 (blue stars) and Obs-QSO (red circles) samples. Uncertainties are estimated from bootstrap resampling. Data points for the two quasar types are slightly offset for clarity. The angular correlation function for DM, evaluated for the redshift distributions of the galaxies and the QSO-1s, is shown by the dotted gray line, and power-law fits (with fixed $\delta = 0.8$) are shown as solid blue and red lines. All fits are performed over the range in separation of $1'$ to $12'$.

(A color version of this figure is available in the online journal.)

The resulting cross-correlations and scaled DM fits are shown in Figure 9, and fit parameters are given in Table 1. The estimates of r_0 and $b_Q b_G$ are in broad agreement between the two estimators, although as may be expected, the statistical uncertainties for the angular correlation analysis are larger (by $\sim$50%) than for the real-space analysis with fixed γ. Given that the absolute bias derived from the projected correlation function corresponds broadly to the bias from the noisier, but simpler angular cross-correlation, we conclude that there are no significant systematic effects that skew our estimate of $w_p(R)$.

6.2. Variation in $w_p(R)$ with Redshift

Our calculation of the real-space quasar–galaxy correlation function over the redshift range $0.7 < z < 1.8$ requires that $w_p(R)$ varies only slowly between these redshifts, as discussed in Section 4.2. If the objects reside in similar halos at all redshifts, then we may expect r_0 to change slowly; simulations suggest that the typical r_0 for the autocorrelation of DM halos of mass $\sim 10^{12}$–$10^{13}\,h^{-1}\,M_\odot$ should change by $\lesssim 0.2\,h^{-1}$ Mpc between $z = 0.5$ and 2 (see Figure 10 of Starikova et al. 2010). To test explicitly the redshift variation for the clustering in our sample, we re-derived $w_p(R)$ using the method outlined in Section 4 but selecting quasars over smaller redshift bins of $0.7 < z < 1.25$ and $1.25 < z < 1.8$. Uncertainties are calculated using the bootstrap method as for the full quasar samples, and DM and power-law fits are again performed over the range of separations $0.3 < R < 12\,h^{-1}$ Mpc. We evaluate $w_p^{DM}(R)$ as in Section 4.7, but only including the quasars in the redshift ranges of interest. Owing to larger statistical errors and for simple comparison to the results over the full redshift range, in the power-law fits we fix γ to 1.8.

The resulting $w_p(R)$ for the separate redshift bins and the power-law fits are shown in Figure 10. For the QSO-1s, we obtain $r_0 = 5.1 \pm 0.8\,h^{-1}$ Mpc and $6.3 \pm 0.7\,h^{-1}$ Mpc for the low- and high-redshift bins, respectively, and for the Obs-QSOs we correspondingly obtain $r_0 = 6.2 \pm 0.7\,h^{-1}$ Mpc

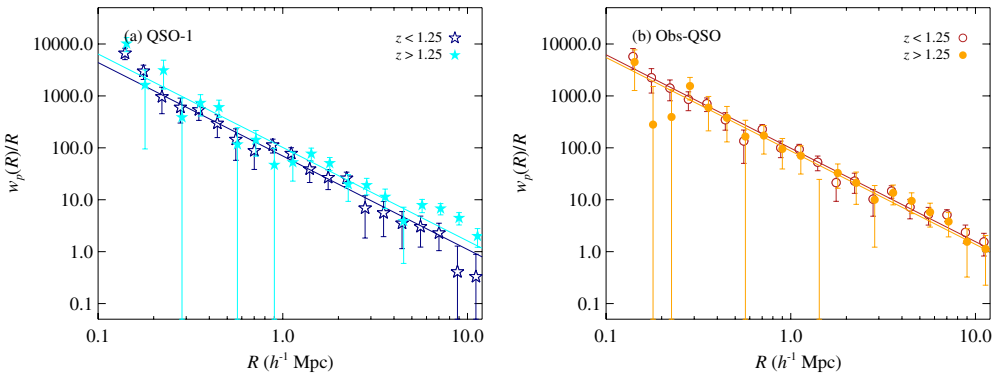

Figure 10. Projected quasar–galaxy cross-correlation function in two redshift bins: $0.7 < z < 1.25$ and $1.25 < z < 1.8$, with symbols shown as in the upper right. Data points for the two redshift bins are slightly offset for clarity. Power-law fits with γ fixed to 1.8 are shown as solid lines, with colors corresponding to the symbols for each redshift bin. Any variation in $w_p(R)$ with redshift is relatively weak, confirming that the method outlined in Section 4.2 should be valid for this analysis. Note that for the Obs-QSOs at $z > 1.25$, we exclude the bin with $w_p(R) < 0$, which disproportionately affects the fit. (Including this bin decreases the clustering amplitude by ≈20%.) Fit parameters are DM halo masses for each redshift bin are given in Table 1.

(A color version of this figure is available in the online journal.)

and $5.8 \pm 1.0\,h^{-1}$ Mpc. The measured quasar–galaxy cross-correlation should be largely independent between the two redshift bins. Although the quasars are cross-correlated against the same galaxy sample in each bin, the galaxy samples will be weighted toward higher and lower redshifts in the high- and low-z bins, respectively. For the high- and low-redshift bins, the best-fit r_0 values bracket those for the full redshift samples, are broadly consistent within the uncertainties. Interestingly, the best-fit clustering amplitude for the Obs-QSOs increases with redshift while it decreases for the Obs-QSOs; however, given the uncertainties we decline to speculate on any possible difference in redshift evolution between the two subsets. Overall, the results in the different redshift bins confirm that any variation in the observed $w_p(R)$ is sufficiently weak over the redshift range of interest, so that the method outlined in Section 4.2 should provide a reasonable estimate of the average clustering amplitude over the full redshift range.

6.3. Effects of Quasar Photo-z Errors

The primary uncertainty in our estimate of $w_p(R)$ for the Obs-QSOs is the lack of accurate (that is, spectroscopic) redshifts and difficulty in estimating the photo-z uncertainties from the neural net calculations. As described in Section 4, in calculating $w_p(R)$ for the Obs-QSO–galaxy cross-correlation, we simply assume that Obs-QSOs lie exactly at the best redshifts output by the neural net estimator. Any uncertainties in the photo-zs or systematic offsets from the true redshifts could therefore affect the resulting clustering measurement. The fact that we obtain very similar estimates of b_Q for the Obs-QSOs from a simple angular cross-correlation analysis as from our $w_p(R)$ calculation suggests that uncertainties on individual photo-zs do not strongly affect our estimates of the quasar bias, as long as the overall distribution in redshifts for the Obs-QSOs is correct. However, it is possible that very large discrepancies from the true photo-zs, or any systematic shift in the redshift distribution, could affect both the estimate of $w_p(R)$ and the real-space clustering parameters derived from $\omega(\theta)$.

To precisely explore the effect of these errors, we take advantage of the fact that we have an equivalent sample of objects (the QSO-1s) that have a similar redshift distribution and for which the redshifts are known precisely from spectroscopy. We can therefore adjust the redshifts of the QSO-1s and recalculate $w_p(R)$ to determine how uncertainties or systematic

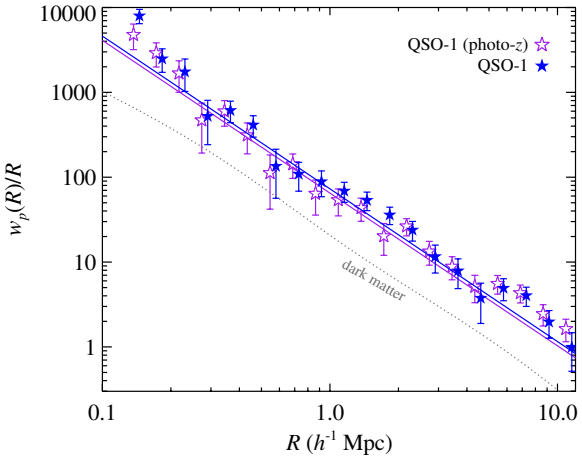

Figure 11. Projected quasar–galaxy cross-correlation function for QSO-1s, using photometric redshifts (purple open stars) and spectroscopic redshifts (blue solid stars). Power-law fits are performed using a fixed $\gamma = 1.8$, and fit parameters are DM halo masses given in Table 1. Using the less accurate (photometric) redshifts has relatively small effect on $w_p(R)$, decreasing the best-fit power-law amplitude by ≈10%.

(A color version of this figure is available in the online journal.)

shifts affect the observed correlation amplitude. As a simple first test, we calculate the $w_p(R)$ for the QSO-1s using the photo-zs (as shown in Figure 4) rather than using spectroscopic redshifts. Figure 11 shows that the resulting $w_p(R)$ differs little from that obtained using spectroscopic redshifts; the clustering amplitude for a power-law fit with fixed $\gamma = 1.8$ is lower by 12%. Note that if we allow γ to float, the average bias for the photo-z sample is actually larger by ≈10% (owing to a slightly flatter slope) but well within the statistical uncertainties. We conclude that for the QSO-1s, photo-z errors do not have a significant effect on our measurements of the clustering.

6.3.1. Random Errors

To explore photo-z errors in more detail, we systematically test the effects of Gaussian random errors in the quasar redshifts. For each quasar, we shift the best estimates of redshift (spec-zs for QSO-1s and photo-zs for Obs-QSOs) by offsets $\Delta z/(1+z)$ selected from a Gaussian random distribution with dispersion $\sigma_z/(1+z)$. Using these new redshifts, we recalculate $w_p(R)$, using the full formalism described in Section 4. We perform

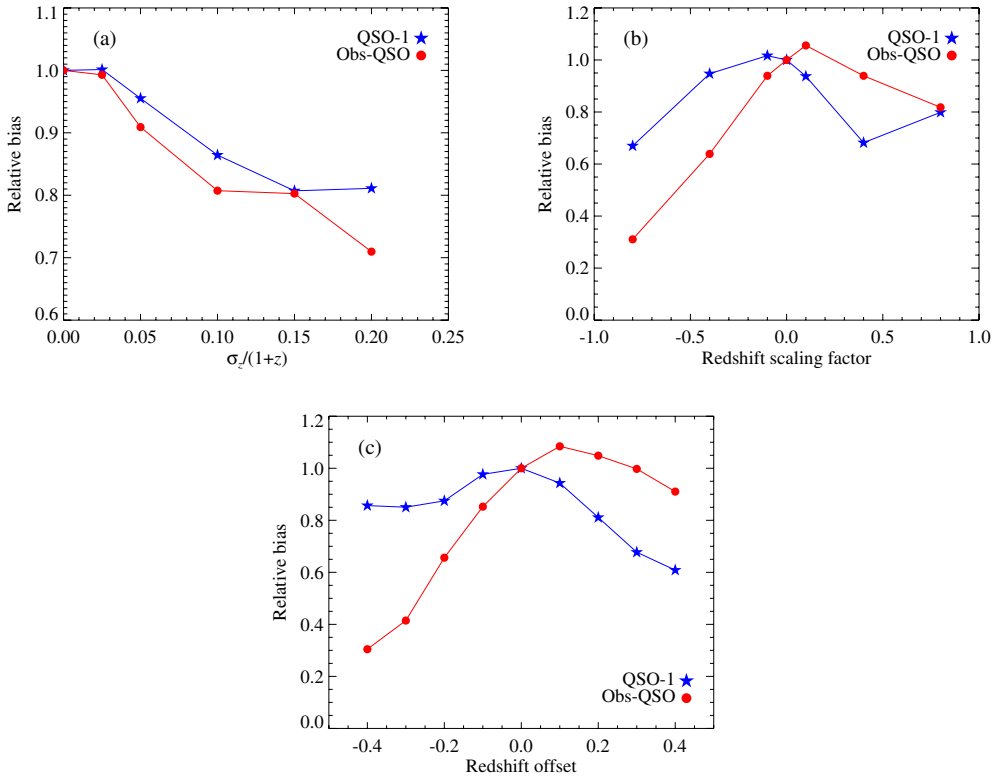

Figure 12. Tests of the effects of redshift errors on the observed clustering, for QSO-1s and Obs-QSOs, as described in Section 6.3. (a) Relative clustering amplitude, after shifting the quasar redshifts by an offset drawn from a Gaussian random distribution with width σ_z. Both types of quasar show a very similar monotonic decrease in clustering amplitude with $\sigma_z/(1+z)$, indicating that the photo-z estimates for the Obs-QSOs are reasonably accurate. (b) Corresponding change in bias after scaling the quasar redshifts toward the limits of the redshift interval $0.7 < z < 1.8$; the scale parameter S_z is defined in Equation (21). (c) Relative bias after a simple upward or downward shift of the quasar redshifts. In both panels (b) and (c), both types of quasar show clustering amplitudes that peak near $S_z = 0$ or $\Delta z = 0$ indicating that there is no large systematic error in the photo-z estimates for the Obs-QSOs.

(A color version of this figure is available in the online journal.)

the calculation 10 times for each of several values of $\sigma_z/(1+z)$ from 0.02 up to 0.2 (which smears the redshifts across most of the redshift range of interest). To ensure that this step does not artificially smear out the redshift distribution beyond the range probed by the galaxies, we require that the random redshifts lie between $0.7 < z < 1.8$; any random redshift that lies outside this range is discarded and a new redshift is selected from the random distribution. For each trial, we obtain the relative bias by calculating the mean ratio of $w_p(R)$, on scales 1–10 h^{-1} Mpc, relative to the $w_p(R)$ for the best estimates of redshift. We then average the 10 trials at each σ_z to obtain a relation between relative bias and σ_z, shown in Figure 12(a).

As may be expected, Figure 12(a) shows that shifting the QSO-1 redshifts from their true values causes a decrease in the cross-correlation amplitude, as the quasars are preferentially correlated with galaxies that are not actually associated in redshift space. We find a monotonic decrease in relative bias with σ_z, from $\approx$0.95 for $\sigma_z/(1+z) = 0.05$ to $\approx$0.8 for $\sigma_z/(1+z) = 0.2$. Repeating this calculation for the Obs-QSOs reveals a very similar trend. The decrease in bias with $\sigma_z/(1+z)$ shown in Figure 12(a) indicates that such errors would affect the measurements of the clustering amplitude by at most $\sim$20%.

6.3.2. Systematic Shifts

While the above analysis suggests that random errors in the Obs-QSO photo-zs do not strongly affect the observed clustering amplitude, it is also possible that systematic uncertainties in the photo-z (consistent over- or under-estimates of the redshift) could significantly alter the observed bias. To test this, we shift the redshifts of the quasars as discussed in Section 6.3.1, but in place of random shifts, we compress all redshifts toward one end or the other of the $0.7 < z < 1.8$ range. (This procedure allows us to test the effects of systematic shifts in redshift while keeping the same overall redshift range.) The shift in redshift is defined by a redshift scaling parameter S_z, such that

$$z_{\rm new} = \begin{cases} z + S_z(z - 0.7) & S_z < 0 \\ z + S_z(1.8 - z) & S_z \geqslant 0. \end{cases} \quad (21)$$

As an additional check we also perform a simple linear offset Δz of the redshifts, allowing the redshifts to move outside the selection range of $0.7 < z < 1.8$. As in Section 6.3.1, we use these new redshifts to recalculate $w_p(R)$ via the full formalism described in Section 4, and determine the relative bias on scales 1–10 h^{-1} Mpc. Relative bias versus S_z and Δz are shown in Figures 12(b) and (c). For the QSO-1s, the peak of the observed clustering amplitude is very close to $S_z = 0$, while shifting the redshifts down or up systematically decreases the bias. The Obs-QSOs show a similar peak near $S_z = 0$, indicating that the Obs-QSO photo-zs are not systematically offset higher or lower than the true redshifts by a large factor. We note that for the Obs-QSOs, a slight shift to higher redshifts ($\Delta z = 0.1$) increases the clustering by a small amount ($\approx$8%).

Finally, we emphasize that any possible low-redshift contaminants (such as star-forming galaxies, as discussed in Section 7

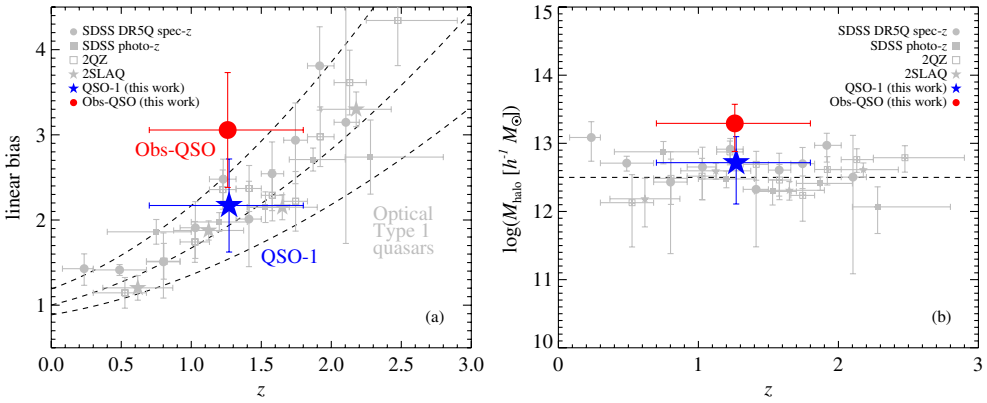

Figure 13. Comparison of (a) linear bias and (b) inferred DM halo mass to previous measurements of Type 1 quasar clustering. Lines in the left plot correspond to the linear bias for DM halos with $\log M_{\rm halo}[h^{-1}\,M_{\odot}] = 12.0$, 12.5, and 13.0 (from bottom to top). The gray points show results from quasar–quasar correlation measurements using spectroscopic samples from SDSS (Ross et al. 2009), 2QZ (Croom et al. 2005), and 2SLAQ (da Ângela et al. 2008), as well as the clustering of photometrically selected quasars from SDSS (Myers et al. 2006). The blue star and red circle show our measurements for QSO-1s and Obs-QSOs, respectively. Our QSO-1 measurement agrees closely with previous work on Type 1 quasar–quasar correlations, while the Obs-QSOs show marginally $\approx 1\sigma$ stronger clustering, corresponding to a factor of roughly four in $M_{\rm halo}$.

(A color version of this figure is available in the online journal.)

of H07), will serve only to decrease the observed clustering signal, as they will be completely uncorrelated in angular space with the higher redshift SDWFS galaxies that lie in entirely separate large-scale structures. Therefore, the observed $w_p(R)$ represents a robust lower limit to the clustering amplitude for the Obs-QSOs.

7. DISCUSSION

We have used the IR-selected quasar sample of H07 to measure the clustering amplitude and to estimate characteristic DM halo masses for roughly equivalent samples of unobscured and obscured quasars. We obtain highly significant detections of the clustering for both samples, with marginally stronger clustering for the Obs-QSOs. In this section, we compare our results for QSO-1s to previous results on unobscured quasar clustering, speculate on physical explanations for possible stronger clustering for Obs-QSOs, and discuss prospects for future studies with the next generation of observatories.

7.1. Comparison with Previous Results

We compare our observed absolute bias for the mid-IR-selected quasars with the clustering of optically selected (Type 1) quasars, which has been well established by a number of works. Among the most precise measurements to date are studies that have used data from the 2dF and SDSS surveys. Recently, Ross et al. (2009) measured the evolution of the quasar three-dimensional autocorrelation function based on spectroscopic quasars from SDSS Data Release 5, and compared to previous results from spectroscopic samples from the 2QZ (Croom et al. 2005) and 2SLAQ (da Ângela et al. 2008), as well as the clustering of photometrically selected quasars from SDSS (Myers et al. 2006). Figure 13(a) shows the redshift evolution of linear bias for Type 1 quasars from these studies, taken from Figure 12 of Ross et al. (2009). Where appropriate, we have converted the bias to our adopted cosmology using the formalism in the Appendix of Starikova et al. (2010), assuming a shape factor $s = 1$ for simplicity. Figure 13(b) shows the corresponding estimates of characteristic $M_{\rm halo}$ derived from the linear bias using the prescription of Sheth et al. (2001). The linear bias and halo masses for the QSO-1s and Obs-QSOs are shown for comparison.

It is readily apparent from Figure 13(a) that the observed bias of Type 1 quasars increases with redshift, as discussed in Section 1. (These results are also consistent with a number of other quasar clustering studies using other data see, e.g., Figure 15 of Hopkins et al. 2008.) The dashed curves in Figure 13(a) show the increase in bias with redshift for halos of constant mass, clearly showing that at all redshifts the QSO-1s reside in DM halos of roughly a few $\times 10^{12}\ h^{-1}\,M_{\odot}$. Our measurement for the QSO-1s is in excellent agreement with the evolution in linear bias and roughly constant $M_{\rm halo}$ observed in previous measurements of Type 1 quasar clustering.

For the Obs-QSOs, the best-fit bias is marginally larger ($\approx 1\sigma$), corresponding to a factor of roughly four difference in the characteristic $M_{\rm halo}$ between the QSO-1s and Obs-QSOs (Figure 13(b)). As discussed above, random errors in the photo-zs can only decrease the observed clustering amplitude and the inferred $M_{\rm halo}$. Thus, our measurement of Obs-QSO clustering represents a lower limit, and it is possible that the true Obs-QSO bias is somewhat higher (although the results of Section 6 suggest that the true bias may be larger by at most $\sim$20%). Based on this analysis we can make the robust conclusion that the Obs-QSOs are *at least* as strongly clustered as their QSO-1 counterparts.

7.2. Physical Implications

Stronger clustering for obscured quasars would have significant implications for physical models of the obscured quasar population. In terms of unified models, a difference in clustering between obscured and unobscured quasars would rule out the simplest picture in which obscuration is purely an orientation effect, but may be consistent with more complicated scenarios where the effective covering fraction changes with environment. Alternatively, if obscuration is caused by large ($\sim$kpc scale) structures, then the processes that drive these asymmetries (e.g., mergers, disk instabilities, accretion of cold gas from the surrounding halo) may be more common in halos of larger mass. Indeed, given that some fraction of quasars might naturally be expected to be obscured by a "unified"-model torus, any observed differences in clustering may reflect even stronger intrinsic dependence of large-scale obscuration and environment.

An intriguing scenario for obscured quasars is that they represent an early evolutionary phase of rapid black hole growth before a "blowout" of the obscuring material from the central regions of the galaxy and the emergence of an unobscured quasar (e.g., Figure 1 of Hopkins et al. 2008). Quasars tend to radiate at large fraction of the Eddington rate (McLure & Dunlop 2004; Kollmeier et al. 2006; although see Kelly et al. 2010), so that the similar $L_{\rm bol}$ for QSO-1s and Obs-QSOs would imply that they host black holes of similar masses. Any correlation (e.g., Ferrarese 2002; Booth & Schaye 2010), even if indirect (e.g., Kormendy & Bender 2011), between the final masses of black holes and those of their host halos would thus suggest that our obscured and unobscured quasars would have the same $M_{\rm halo}$, as long as their black holes are near their final masses. However, if obscured quasars are in an earlier phase of rapid growth and so are in the process of "catching up" to their final mass (e.g., King 2010), then they would have a larger $M_{\rm halo}$ compared to unobscured quasars with the same $M_{\rm BH}$. In light of recent debate as to whether black holes generally grow before or after their hosts (e.g., Peng et al. 2006; Alexander et al. 2008; Woo et al. 2008; Decarli et al. 2010), this scenario would imply that black hole growth lags behind that of the host halo.

In any physical picture, a significant difference in clustering between obscured and unobscured quasars would also imply a difference in accretion duty cycles (or equivalently, lifetime). QSO-1s and Obs-QSOs are found in roughly equal numbers, but the abundance of DM halos drops rapidly with mass (e.g., Jenkins et al. 2001), thus implying that if one type of quasars are found in larger halos then they must be longer-lived. With our current results, we are able to rule out any model in which obscured quasars are substantially *less* strongly clustered or have *shorter* lifetimes than their unobscured counterparts. With more accurate future measurements, detailed studies of halo masses and lifetimes for obscured and unobscured quasars could place powerful constraints on evolutionary scenarios such as those described above.

7.3. Future Prospects

Our results demonstrate the potential for studying the clustering of obscured quasars in extragalactic multiwavelength surveys, and the marginally significant difference in clustering we observe for obscured and unobscured quasars provides strong motivation for more precise measurements in the future. The two main avenues for progress are improvements in redshift accuracy and selection of larger samples for better statistical accuracy. Upcoming sensitive, wide-field multi-object spectrographs will enable efficient measurements of redshift for large numbers of optically faint sources and so improve calibrations of obscured quasar photo-zs, or with large enough samples enable fully three-dimensional clustering studies. In addition, we will soon have the capability to detect many thousands of obscured quasars based on very wide-field observations in the mid-IR with the *Wide-Field Infrared Survey Explorer* (Wright 2010) and in X-rays with eROSITA (Predehl et al. 2007) or the *Wide-Field X-ray Telescope* (Murray et al. 2010). These data sets will allow us to measure obscured quasar clustering with statistical precision that is comparable to current measurements of unobscured quasars.

8. SUMMARY

We have used data from the Boötes wide-field multiwavelength survey to measure the two-point spatial cross-correlation between unobscured (QSO-1) and obscured (Obs-QSO) mid-IR-selected quasars in the redshift range $0.7 < z < 1.8$. The QSO-1s exhibit clustering corresponding to a typical $M_{\rm halo} \sim 5 \times 10^{12}\ h^{-1}\ M_{\odot}$, similar to previous studies of optically selected quasar clustering. We robustly determine that the Obs-QSOs are clustered *at least* as strongly as the QSO-1s, with a marginally stronger signal corresponding to host halos of mass $\sim 2 \times 10^{13}\ h^{-1}\ M_{\odot}$; the true clustering amplitude could be up to $\sim$20% larger owing to photo-z uncertainties for the Obs-QSOs that can decrease the observed correlation amplitude. Our results motivate more accurate measurements of obscured quasar clustering with larger quasar samples and more accurate redshifts. If future studies confirm that obscured quasars are more strongly clustered than their unobscured counterparts, this would rule out the simplest "unified" models and may provide evidence for scenarios in which rapid obscured accretion represents an evolutionary phase in the growth of galaxies and their central black holes.

We thank our colleagues on the NDWFS, AGES, SDWFS, and XBoötes teams. We thank the anonymous referee for helpful comments that improved the paper, and Philip Hopkins and Peder Norberg for productive discussions. The NOAO Deep Wide-field Survey, and the research of A.D. and B.T.J. are supported by NOAO, which is operated by the Association of Universities for Research in Astronomy (AURA), Inc. under a cooperative agreement with the National Science Foundation. This paper would not have been possible without the efforts of the *Chandra*, *Spitzer*, KPNO, and MMT support staff. Optical spectroscopy discussed in this paper was obtained at the MMT Observatory, a joint facility of the Smithsonian Institution and the University of Arizona. The first *Spitzer* MIPS survey of the Boötes region was obtained using GTO time provided by the *Spitzer* Infrared Spectrograph Team (PI: James Houck) and by M. Rieke. We thank the collaborators in that work for access to the 24 micron catalog generated from those data. R.C.H. was supported by an STFC Postdoctoral Fellowship and an SAO Postdoctoral Fellowship, and A.D.M. was generously funded by the NASA ADAP program under grant NNX08AJ28G. D.M.A. is grateful to the Royal Society and Philip Leverhulme Prize for their generous support. R.J.A. was supported by the NASA Postdoctoral Program, administered by Oak Ridge Associated Universities through a contract with NASA.

APPENDIX

EDGE EFFECTS AND CORRELATIONS ON LARGE SCALES

The large area of the Boötes survey allows us to measure galaxies at relatively large physical separations; 1 degree corresponds to 50 h^{-1} Mpc at $z = 1.5$. However, when we use Equation (7) to calculate the projected real-space correlation function on large scales, we find that the $w_p(R)$ flattens on scales $R \sim$ 10–20 h^{-1} Mpc, corresponding to tens of arcmin, and then becomes negative at $R \sim 100\,h^{-1}$ Mpc (Figure 14). This behavior is not observed for quasar clustering from other wider-field surveys (e.g., Croom et al. 2005; Myers et al. 2009), for which the correlation function continues to decrease on larger scales. While the integral constraint requires that the correlation function become negative on some scales, in galaxy auto-correlation surveys this generally only happens at $R \gtrsim 200\ h^{-1}$ Mpc (e.g., Eisenstein et al. 2005).

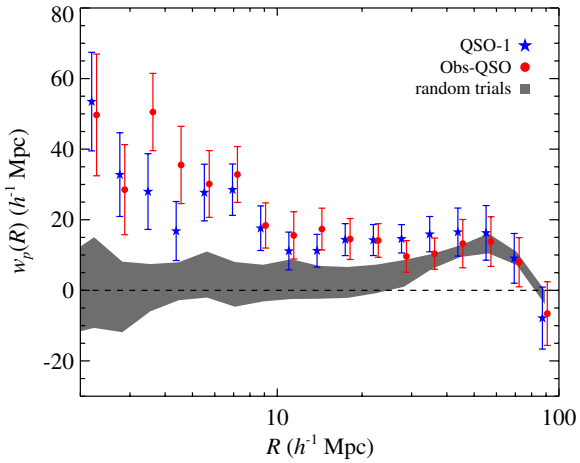

Figure 14. Observed projected cross-correlation between quasars and galaxies derived using Equation (7) (blue stars and red circles for QSO-1s and Obs-QSOs, respectively), compared to the same quantity but derived for samples of quasars with the redshifts equal to those of the QSO-1s but with randomized sky positions. The gray shaded region shows the dispersion between 10 different random quasar samples. Note that the correlation between random quasars and galaxies is small relative to the real-quasar galaxy correlation, except on scales >10–$20\,h^{-1}$ Mpc where both quantities show a hump and then become negative. This feature is likely due to edge effects in the finite SDWFS field, as discussed in the Appendix. Because of this artifact we restrict our correlation analyses to $R < 12\,h^{-1}$ Mpc.

(A color version of this figure is available in the online journal.)

One possibility is that the observed behavior is due to edge effects arising from the finite geometry of the SDWFS field, which are not taken into account by the simple $\xi(R) = DD/DR - 1$ estimator in the M09 formalism (e.g., Landy & Szalay 1993). To test this possibility, we reperformed the correlation analysis described in Section 4, after randomizing the positions of the quasars on the sky within the area of good SDWFS photometry. We performed 10 separate random trials, for which the cross-correlations are shown in Figure 14 along with the $w_p(R)$ values for the QSO-1s and Obs-QSOs. It is clear from Figure 14 that on scales $\lesssim 10\,h^{-1}$ Mpc, the projected cross-correlation between the random quasars and galaxies is small compared to the $w_p(R)$ for the real quasar sample. However, on scales $\gtrsim 20\ h^{-1}$ Mpc, both the real and random samples show an increase in $w_p(R)$ which eventually becomes negative around $R = 100\,h^{-1}$ Mpc. The quantities of interest in this paper (i.e., absolute bias and DM halo mass) can be measured by studying the correlations on scales $<12\ h^{-1}$ Mpc, where the artifacts are small and have negligible impact on the fits to the correlation function. For this paper, we therefore limit the correlation analyses to those scales.

REFERENCES

Adelberger, K. L., & Steidel, C. C. 2005, ApJ, 630, 50
Alexander, D. M., Brandt, W. N., Hornschemeier, A. E., Garmire, G. P., Schneider, D. P., Bauer, F. E., & Griffiths, R. E. 2001, AJ, 122, 2156
Alexander, D. M., et al. 2008, AJ, 135, 1968
Alonso-Herrero, A., et al. 2006, ApJ, 640, 167
Antonucci, R. 1993, ARA&A, 31, 473
Ashby, M. L. N., et al. 2009, ApJ, 701, 428
Assef, R. J., et al. 2010, ApJ, 713, 970
Assef, R. J., et al. 2011, ApJ, 728, 56
Baugh, C. M., & Efstathiou, G. 1993, MNRAS, 265, 145
Bertin, E., & Arnouts, S. 1996, A&AS, 117, 393
Booth, C. M., & Schaye, J. 2010, MNRAS, 405, L1
Bower, R. G., Benson, A. J., Malbon, R., Helly, J. C., Frenk, C. S., Baugh, C. M., Cole, S., & Lacey, C. G. 2006, MNRAS, 370, 645
Brodwin, M., et al. 2006, ApJ, 651, 791
Brodwin, M., et al. 2008, ApJ, 687, L65
Brown, M. J. I., et al. 2008, ApJ, 682, 937
Ciotti, L., & Ostriker, J. P. 2007, ApJ, 665, 1038
Ciotti, L., Ostriker, J. P., & Proga, D. 2010, ApJ, 717, 708
Coil, A. L., Hennawi, J. F., Newman, J. A., Cooper, M. C., & Davis, M. 2007, ApJ, 654, 115
Coil, A. L., et al. 2008, ApJ, 672, 153
Coil, A. L., et al. 2009, ApJ, 701, 1484
Comastri, A., Setti, G., Zamorani, G., & Hasinger, G. 1995, A&A, 296, 1
Conroy, C., & Wechsler, R. H. 2009, ApJ, 696, 620
Constantin, A., & Vogeley, M. S. 2006, ApJ, 650, 727
Croom, S. M., Smith, R. J., Boyle, B. J., Shanks, T., Miller, L., Outram, P. J., & Loaring, N. S. 2004, MNRAS, 349, 1397
Croom, S. M., et al. 2005, MNRAS, 356, 415
da Ângela, J., et al. 2008, MNRAS, 383, 565
Decarli, R., Falomo, R., Treves, A., Labita, M., Kotilainen, J. K., & Scarpa, R. 2010, MNRAS, 402, 2453
Dey, A., et al. 2008, ApJ, 677, 943
Donley, J. L., Rieke, G. H., Pérez-González, P. G., Rigby, J. R., & Alonso-Herrero, A. 2007, ApJ, 660, 167
Donoso, E., Li, C., Kauffmann, G., Best, P. N., & Heckman, T. M. 2010, MNRAS, 407, 1078
Efstathiou, G., Bernstein, G., Tyson, J. A., Katz, N., & Guhathakurta, P. 1991, ApJ, 380, L47
Eisenhardt, P. R., et al. 2004, ApJS, 154, 48
Eisenstein, D. J., et al. 2005, ApJ, 633, 560
Elvis, M., et al. 1994, ApJS, 95, 1
Fabricant, D., et al. 2005, PASP, 117, 1411
Fan, X., et al. 2006, AJ, 131, 1203
Ferrarese, L. 2002, ApJ, 578, 90
Gandhi, P., et al. 2006, A&A, 457, 393
Genzel, R., et al. 2008, ApJ, 687, 59
Gilli, R., Comastri, A., & Hasinger, G. 2007a, A&A, 463, 79
Gilli, R., et al. 2007b, A&A, 475, 83
Gilli, R., et al. 2009, A&A, 494, 33
Gorjian, V., et al. 2008, ApJ, 679, 1040
Greene, J. E., Zakamska, N. L., Ho, L. C., & Barth, A. J. 2011, ApJ, in press (arXiv:1102.2913)
Groth, E. J., & Peebles, P. J. E. 1977, ApJ, 217, 385
Haas, M., Willner, S. P., Heymann, F., Ashby, M. L. N., Fazio, G. G., Wilkes, B. J., Chini, R., & Siebenmorgen, R. 2008, ApJ, 688, 122
Hickox, R. C., et al. 2007, ApJ, 671, 1365
Hickox, R. C., et al. 2009, ApJ, 696, 891
Hopkins, P. F., & Hernquist, L. 2006, ApJS, 166, 1
Hopkins, P. F., Hernquist, L., Cox, T. J., Di Matteo, T., Robertson, B., & Springel, V. 2006a, ApJS, 163, 1
Hopkins, P. F., Hernquist, L., Cox, T. J., & Kereš, D. 2008, ApJS, 175, 356
Hopkins, P. F., Richards, G. T., & Hernquist, L. 2007, ApJ, 654, 731
Hopkins, P. F., Somerville, R. S., Hernquist, L., Cox, T. J., Robertson, B., & Li, Y. 2006b, ApJ, 652, 864
Jannuzi, B. T., & Dey, A. 1999, in ASP Conf. Ser. 191, Photometric Redshifts and the Detection of High Redshift Galaxies, ed. R. Weymann, L. Storrie-Lombardi, M. Sawicki, & R. Brunner (San Francisco, CA: ASP), 111
Jenkins, A., Frenk, C. S., White, S. D. M., Colberg, J. M., Cole, S., Evrard, A. E., Couchman, H. M. P., & Yoshida, N. 2001, MNRAS, 321, 372
Kauffmann, G., & Haehnelt, M. 2000, MNRAS, 311, 576
Kelly, B. C., Vestergaard, M., Fan, X., Hopkins, P., Hernquist, L., & Siemiginowska, A. 2010, ApJ, 719, 1315
Kenter, A., et al. 2005, ApJS, 161, 9
Kim, J., Edge, A. C., Wake, D. A., & Stott, J. P. 2011, MNRAS, 410, 241
King, A. R. 2010, MNRAS, 408, L95
Kollmeier, J. A., et al. 2006, ApJ, 648, 128
Kormendy, J., & Bender, R. 2011, Nature, 469, 377
Kormendy, J., & Richstone, D. 1995, ARA&A, 33, 581
Krumpe, M., Miyaji, T., & Coil, A. L. 2010, ApJ, 713, 558
Lacy, M., et al. 2004, ApJS, 154, 166
Landy, S. D., & Szalay, A. S. 1993, ApJ, 412, 64
Li, C., Kauffmann, G., Wang, L., White, S. D. M., Heckman, T. M., & Jing, Y. P. 2006, MNRAS, 373, 457
Limber, D. N. 1953, ApJ, 117, 134
Mainieri, V., et al. 2005, A&A, 437, 805
Mandelbaum, R., Li, C., Kauffmann, G., & White, S. D. M. 2009, MNRAS, 393, 377
Marconi, A., Risaliti, G., Gilli, R., Hunt, L. K., Maiolino, R., & Salvati, M. 2004, MNRAS, 351, 169

Martínez-Sansigre, A., Rawlings, S., Lacy, M., Fadda, D., Jarvis, M. J., Marleau, F. R., Simpson, C., & Willott, C. J. 2006, MNRAS, 370, 1479
Martínez-Sansigre, A., et al. 2009, ApJ, 706, 184
McCarthy, P. J. 1993, ARA&A, 31, 639
McLure, R. J., & Dunlop, J. S. 2004, MNRAS, 352, 1390
Merloni, A., & Heinz, S. 2008, MNRAS, 388, 1011
Mo, H. J., Mao, S., & White, S. D. M. 1998, MNRAS, 295, 319
Mountrichas, G., Sawangwit, U., Shanks, T., Croom, S. M., Schneider, D. P., Myers, A. D., & Pimbblet, K. 2009, MNRAS, 394, 2050
Murray, S., et al. 2010, in AIP Conf. Ser. 1248, X-ray Astronomy 2009: Present Status, Multi-wavelength Approach and Future Perspectives, ed. A. Comastri, L. Angelini, & M. Cappi (Melville, NY: AIP), 549
Myers, A. D., Brunner, R. J., Nichol, R. C., Richards, G. T., Schneider, D. P., & Bahcall, N. A. 2007, ApJ, 658, 85
Myers, A. D., White, M., & Ball, N. M. 2009, MNRAS, 399, 2279
Myers, A. D., et al. 2006, ApJ, 638, 622
Norberg, P., Baugh, C. M., Gaztañaga, E., & Croton, D. J. 2009, MNRAS, 396, 19
Padmanabhan, N., White, M., Norberg, P., & Porciani, C. 2009, MNRAS, 397, 1862
Page, M. J., Stevens, J. A., Ivison, R. J., & Carrera, F. J. 2004, ApJ, 611, L85
Peacock, J. A. 1991, MNRAS, 253, 1P
Peebles, P. J. E. 1980, The Large-scale Structure of the Universe (Princeton, NJ: Princeton Univ. Press)
Peng, C. Y., Impey, C. D., Rix, H.-W., Kochanek, C. S., Keeton, C. R., Falco, E. E., Lehár, J., & McLeod, B. A. 2006, ApJ, 649, 616
Polletta, M. d. C., et al. 2006, ApJ, 642, 673
Porciani, C., Magliocchetti, M., & Norberg, P. 2004, MNRAS, 355, 1010
Predehl, P., et al. 2007, in Proc. SPIE, 6686, 668617
Ptak, A., Zakamska, N. L., Strauss, M. A., Krolik, J. H., Heckman, T. M., Schneider, D. P., & Brinkmann, J. 2006, ApJ, 637, 147
Quadri, R. F., Williams, R. J., Lee, K., Franx, M., van Dokkum, P., & Brammer, G. B. 2008, ApJ, 685, L1
Reyes, R., et al. 2008, AJ, 136, 2373
Richards, G. T., et al. 2001, AJ, 121, 2308
Richards, G. T., et al. 2005, MNRAS, 360, 839
Richards, G. T., et al. 2006, ApJS, 166, 470
Richards, G. T., et al. 2009a, AJ, 137, 3884
Richards, G. T., et al. 2009b, ApJS, 180, 67
Ross, N. P., et al. 2009, ApJ, 697, 1634
Rowan-Robinson, M., et al. 2005, AJ, 129, 1183
Schneider, D. P., et al. 2007, AJ, 134, 102
Serber, W., Bahcall, N., Ménard, B., & Richards, G. 2006, ApJ, 643, 68
Seymour, N., et al. 2007, ApJS, 171, 353
Shankar, F., Weinberg, D. H., & Miralda-Escudé, J. 2009, ApJ, 690, 20
Shanks, T., Bean, A. J., Ellis, R. S., Fong, R., Efstathiou, G., & Peterson, B. A. 1983, ApJ, 274, 529
Shen, Y., et al. 2007, AJ, 133, 2222
Sheth, R. K., Mo, H. J., & Tormen, G. 2001, MNRAS, 323, 1
Silk, J., & Rees, M. J. 1998, A&A, 331, L1
Smith, R. E., et al. 2003, MNRAS, 341, 1311
Soltan, A. 1982, MNRAS, 200, 115
Spergel, D. N., et al. 2007, ApJS, 170, 377
Springel, V., Di Matteo, T., & Hernquist, L. 2005, MNRAS, 361, 776
Starikova, S., et al. 2010, ApJ, submitted (arXiv:1010.1577)
Stern, D., et al. 2002, ApJ, 568, 71
Stern, D., et al. 2005, ApJ, 631, 163
Tinker, J. L., Weinberg, D. H., Zheng, Z., & Zehavi, I. 2005, ApJ, 631, 41
Tinker, J. L., & Wetzel, A. R. 2010, ApJ, 719, 88
Treister, E., et al. 2004, ApJ, 616, 123
Urry, C. M., & Padovani, P. 1995, PASP, 107, 803
Vignali, C., Alexander, D. M., & Comastri, A. 2006, MNRAS, 373, 321
Vignali, C., Alexander, D. M., Gilli, R., & Pozzi, F. 2010, MNRAS, 404, 48
Vignali, C., et al. 2009, MNRAS, 395, 2189
Wake, D. A., Croom, S. M., Sadler, E. M., & Johnston, H. M. 2008, MNRAS, 391, 1674
Woo, J., Treu, T., Malkan, M. A., & Blandford, R. D. 2008, ApJ, 681, 925
Wright, E. L., et al. 2010, AJ, 140, 1868
Yu, Q., & Tremaine, S. 2002, MNRAS, 335, 965
Zakamska, N. L., Strauss, M. A., Heckman, T. M., Ivezić, Ž., & Krolik, J. H. 2004, AJ, 128, 1002
Zakamska, N. L., et al. 2003, AJ, 126, 2125
Zakamska, N. L., et al. 2005, AJ, 129, 1212
Zehavi, I., et al. 2004, ApJ, 608, 16
Zehavi, I., et al. 2005, ApJ, 630, 1
Zheng, Z., Coil, A. L., & Zehavi, I. 2007, ApJ, 667, 760
Zheng, Z., Zehavi, I., Eisenstein, D. J., Weinberg, D. H., & Jing, Y. P. 2009, ApJ, 707, 554